NeuroImage 78 (2013) 16–32

Contents lists available at SciVerse ScienceDirect

NeuroImage

journal homepage: www.elsevier.com/locate/ynimg

Mean apparent propagator (MAP) MRI: A novel diffusion imaging method for mapping tissue microstructure

Evren Özarslan [a,b,c,*], Cheng Guan Koay [d], Timothy M. Shepherd [e], Michal E. Komlosh [a,b], M. Okan İrfanoğlu [a,b], Carlo Pierpaoli [a], Peter J. Basser [a]

[a] Section on Tissue Biophysics and Biomimetics, PPITS, NICHD, National Institutes of Health, Bethesda, MD 20892, USA
[b] Center for Neuroscience and Regenerative Medicine, Uniformed Services University of the Health Sciences, Bethesda, MD 20814, USA
[c] Department of Radiology, Brigham and Women's Hospital, Harvard Medical School, Boston, MA 02215, USA
[d] Department of Medical Physics, University of Wisconsin, Madison, WI 53705, USA
[e] Department of Radiology, New York University Langone Medical Center, New York, NY 10016, USA

ARTICLE INFO

Article history:
Accepted 2 April 2013
Available online 13 April 2013

Keywords:
Diffusion
Propagator
ODF
Return-to-origin
Non-Gaussianity
Anisotropy
Volume
Hermite
SHORE
Generalized DTI
GDTI

ABSTRACT

Diffusion-weighted magnetic resonance (MR) signals reflect information about underlying tissue microstructure and cytoarchitecture. We propose a quantitative, efficient, and robust mathematical and physical framework for representing diffusion-weighted MR imaging (MRI) data obtained in "*q*-space," and the corresponding "mean apparent propagator (MAP)" describing molecular displacements in "*r*-space." We also define and map novel quantitative descriptors of diffusion that can be computed robustly using this MAP-MRI framework.

We describe efficient analytical representation of the three-dimensional *q*-space MR signal in a series expansion of basis functions that accurately describes diffusion in many complex geometries. The lowest order term in this expansion contains a diffusion tensor that characterizes the Gaussian displacement distribution, equivalent to diffusion tensor MRI (DTI). Inclusion of higher order terms enables the reconstruction of the true average propagator whose projection onto the unit "displacement" sphere provides an orientational distribution function (ODF) that contains only the orientational dependence of the diffusion process. The representation characterizes novel features of diffusion anisotropy and the non-Gaussian character of the three-dimensional diffusion process. Other important measures this representation provides include the return-to-the-origin probability (RTOP), and its variants for diffusion in one- and two-dimensions—the return-to-the-plane probability (RTPP), and the return-to-the-axis probability (RTAP), respectively. These zero net displacement probabilities measure the mean compartment (pore) volume and cross-sectional area in distributions of isolated pores irrespective of the pore shape.

MAP-MRI represents a new comprehensive framework to model the three-dimensional *q*-space signal and transform it into diffusion propagators. Experiments on an excised marmoset brain specimen demonstrate that MAP-MRI provides several novel, quantifiable parameters that capture previously obscured intrinsic features of nervous tissue microstructure. This should prove helpful for investigating the functional organization of normal and pathologic nervous tissue.

Introduction

Non-invasive magnetic resonance imaging (MRI) has become paramount to the diagnosis and clinical management of many diseases of the central nervous system (CNS). MRI characterization of tissue water behavior also has contributed significantly to our fundamental understanding of CNS tissue microstructure. Diffusion-weighted MRI (DW-MRI), which is sensitized to the random motion of endogenous water molecules within the tissue environment, has proven particularly important to both clinical and basic science applications.

Conventional DW-MR utilizes two magnetic field gradients (Stejskal and Tanner, 1965) of equal magnitude and direction applied around the 180° radiofrequency (RF) pulse in a spin echo MR sequence. The magnetic moment of a hydrogen nucleus suffers a net phase shift if its locations during the application of the first and second gradients are different. A population of randomly moving nuclei exhibits phase incoherence, which leads to an attenuation in the overall signal. Mathematically, the signal is related to an important quantity, referred to as the propagator, through a Fourier relationship whose inversion yields the expression (Callaghan, 1991; Stejskal, 1965)

$$P(\mathbf{r}) = \int_{\mathcal{R}^3} e^{i2\pi\mathbf{q}\cdot\mathbf{r}} E(\mathbf{q}) d\mathbf{q}, \quad (1)$$

where $P(\mathbf{r})$ denotes the propagator indicating the likelihood for particles to undergo a net displacement $\mathbf{r}$. The reciprocal space vector

* Corresponding author at: Department of Radiology, Brigham and Women's Hospital, Harvard Medical School, Boston, MA 02215, USA.
E-mail address: evren@bwh.harvard.edu (E. Özarslan).

1053-8119/$ – see front matter © 2013 Elsevier Inc. All rights reserved.
http://dx.doi.org/10.1016/j.neuroimage.2013.04.016

$\mathbf{q} = (2\pi)^{-1}\gamma\delta\mathbf{G}$ is an experimentally controlled parameter, where γ is the gyromagnetic ratio, and δ is the duration of the diffusion sensitizing gradients whose magnitude and orientation are determined by $\mathbf{G}$. The normalized signal $E(\mathbf{q})$ is just the ratio of the signal at $\mathbf{q}$ to its value at $\mathbf{q} = 0$.

From a physical point of view, a propagator can be assigned to every location in space and within each voxel. If $P_l(\mathbf{R}, \mathbf{R} + \mathbf{r})$ denotes the local propagator for a spin whose initial and final locations are $\mathbf{R}$ and $\mathbf{R} + \mathbf{r}$, respectively, the MR measurable propagator is given by (Callaghan, 1991; Stejskal, 1965)

$$P(\mathbf{r}) = \int \rho(\mathbf{R}) P_l(\mathbf{R}, \mathbf{R} + \mathbf{r}) d\mathbf{R}, \quad (2)$$

where $\rho(\mathbf{R})$ is the likelihood of finding a spin at location $\mathbf{R}$. Due to the averaging process inherent in the above equation and because the formulation assumes a simple pulse sequence that features a pair of infinitesimally short gradient pulses—conditions often violated to some extent in practice—while neglecting the influence of imaging gradients, we refer to $P(\mathbf{r})$ that is computed through Eq. (1) as the mean apparent propagator (MAP).

From a practical point of view, Eq. (1) suggests that by collecting data at different $\mathbf{q}$-vectors, e.g., by sampling a large Cartesian grid, one can reconstruct the MAP through Eq. (1) using the discrete Fourier transform. This scheme is referred to as q-space imaging (QSI) (Callaghan et al., 1990). The same analysis can be employed for spectroscopy or imaging data, where in the latter case, the transformation is repeated for every voxel of the image, and the results reveal an image of displacement profiles (Callaghan et al., 1988; Wedeen et al., 2005).

Eq. (1) establishes the fundamental relationship between the MR signal and the propagator. Both these functions are strongly influenced by the microscopic environment, which is impossible to resolve through direct MRI due to its limitations in sensitivity. However, if reliable models that link the diffusion process to either of these functions is available, voxel-averaged microscopic descriptors of the medium can be inferred from a collection of MR signals. Such an endeavor typically demands an accurate representation of the signal and/or propagator. For example, parameterizing the small $|\mathbf{q}|$ behavior of the signal profile through an oriented (multivariate) Gaussian function has lead to the introduction of diffusion tensor imaging (DTI) (Basser et al., 1994a). Since then numerous methods have been developed to unravel the complex tissue architecture within each voxel (Aganj et al., 2010; Alexander et al., 2002; Dell'Acqua et al., 2010; Frank, 2002; Jian et al., 2007; Kaden et al., 2007; Liu et al., 2003; Özarslan and Mareci, 2003; Özarslan et al., 2006b; Tournier et al., 2004; Tuch, 2004). Those methods that involve analytical representations of the signal were found to be most convenient as they provide compact representations of the signal as well as the estimated quantities and are inherently less susceptible to the effects of noise; for example, the advantage of an analytical representation was recognized (Anderson, 2005; Descoteaux et al., 2007; Hess et al., 2006) in q-ball imaging whose original realization (Tuch, 2004) lacked such a representation.

The above-mentioned techniques have focused almost exclusively on delineating the orientational features of the diffusion process even when there is more than one major fiber orientation within the voxel—a scenario, which DTI does not account for. However, orientational features, like the orientation distribution function (ODF), constitute only a part of the information that could be obtained from diffusion-attenuated signals. Of particular interest are the features that follow from the restricted character of the diffusion process, which are contained in the full displacement distribution and its dependence on the diffusion time. Such features contain information about cell size, shape, and transmembrane exchange, which are extremely important in biomedical applications of MR, and are obtainable from data acquired at large q-values. To infer such microstructural information and reconstruct the full MAP rather than its orientational features available in the ODF, acquisition of data with three-dimensional q-space coverage is beneficial (Callaghan et al., 1988; Wedeen et al., 2005; Wu and Alexander, 2007). Therefore, the development of a robust analytical model of the signal that could be used to describe data acquired over the entire three-dimensional q-space would be highly useful. To this end, several models have been introduced in recent years to represent the three-dimensional q-space signal (Assemlal et al., 2009, 2011; Cheng et al., 2010; Descoteaux et al., 2011; Hosseinbor et al., 2011; Özarslan et al., 2006b, 2009c; Ozcan, 2010; Ye et al., 2012; Yeh et al., 2011).

In this article, we introduce a new method, referred to as MAP-MRI that subsumes DTI and extends it to generate a true and proper propagator or MAP in each voxel. By quantifying the non-Gaussian character of the diffusion process, this method more accurately characterizes diffusion anisotropy. This technique provides several new quantitative parameters, or MRI "stains," derived from the entire displacement MAP that captures distinct novel features about nervous tissue microstructure. The technique is based on the idea of expressing the three-dimensional q-space MR signal in terms of the eigenfunctions of the quantum-mechanical simple harmonic oscillator (SHO) Hamiltonian, sometimes called the Hermite functions, which have also appeared in the reconstruction of the propagator from its cumulants (Liu et al., 2003, 2004). Estimation of probability distributions in a series of Hermite functions is well-studied in the statistics literature (Schwartz, 1967) and such expansions were shown to possess powerful properties, such as rapid convergence in both real and Fourier spaces (Walter, 1977) that make them ideally suited to problems of q-space signal analysis and mean propagator estimation. This representation is an extension of its one-dimensional (1D) counterpart (Özarslan et al., 2008a), which was shown to accurately represent the signal decay originating from very different environments (from free to restricted). In fact, the 1D version of the method was shown to estimate important microstructural properties such as the moments of the underlying compartment size distribution in a medium composed of isolated pores (Özarslan et al., 2011), and generating temporal scaling contrast (Özarslan et al., 2012) by employing a disordered media model for DW-MR (Özarslan et al., 2006a). We introduced an earlier version of the three-dimensional (3D) formulation in Özarslan et al. (2009c), which was instrumental in evaluating the robustness of sparse and optimal strategies for multiple-shell q-space MRI acquisitions (Koay et al., 2012). Here, we introduce a more refined, general, and comprehensive approach by incorporating an anisotropic scale parameter into the representation, which increases its adaptability to different diffusion profiles. The resulting representation reproduces DTI in its first term, and generalizes it to account for non-Gaussianity in the measured diffusion process.

One-dimensional SHO based reconstruction and estimation (1D-SHORE)

Before we introduce the formulation for representing three-dimensional q-space acquisitions, we examine a considerably simpler problem that involves q-space data obtained with different q-values while the gradient orientation, which defines the x-axis, is fixed. Such acquisitions have been utilized to address a number of important questions in biomedical research (Cohen and Assaf, 2002; Cory and Garroway, 1990). Although the focus of the paper is the modeling framework for three-dimensional acquisitions that will be presented in the following sections, the formulation for the 1D q-space acquisitions has been found to be very useful in several applications (Özarslan et al., 2011, 2012), and here can serve as a pedagogical step before we introduce the more complicated 3D problem.

The q-space signal, obtained from a 1D acquisition as described above, can be written as a function of one variable—the q-value. The central idea of the 1D-SHORE technique is to express such a

diffusion-weighted MR signal profile in a series of basis functions (Özarslan et al., 2008a),

$$S(q) = \sum_{n=0}^{N-1} \tilde{a}_n \phi_n(u,q), \tag{3}$$

with

$$\phi_n(u,q) = \frac{i^{-n}}{\sqrt{2^n n!}} e^{-2\pi^2 q^2 u^2} H_n(2\pi u q), \tag{4}$$

where $H_n(x)$ is the nth order Hermite polynomial and u is a characteristic length that determines the scaling of the functions. In Eq. (3) and throughout the article, the "˜" sign is used to denote coefficients representing the signal prior to normalization. The normalized MR signal attenuation, $E(q) = S(q)/S(0)$, can also be expressed in this basis as

$$E(q) = \sum_{n=0}^{N-1} a_n \phi_n(u,q), \tag{5}$$

where

$$a_n = \frac{\tilde{a}_n}{S_0}, \tag{6}$$

and $S_0 = S(0)$ is the non-diffusion-weighted signal, which can be estimated from the coefficients $\tilde{a}_n$:

$$S_0 = \sum_{n=0}^{N-1} \tilde{a}_n \phi_n(u,0) = \sum_{n=0,2,4,\ldots}^{N-1} \frac{\sqrt{n!}}{n!!} \tilde{a}_n, \tag{7}$$

where $n!! = n \times (n-2) \times (n-4) \times \ldots 2$. It is well-known that the functions ϕ_n form a complete orthogonal basis for the space of square-integrable functions (Ohanian, 1990).

A 1D analog of Eq. (1), given by

$$P_{1D}(x) = \int_{-\infty}^{\infty} e^{i2\pi q x} E(q) dq \tag{8}$$

is frequently employed to transform the 1D q-space signal into a 1D propagator. An important and useful property of the employed basis functions is that their Fourier transforms are also Hermite functions, enabling direct estimation of the 1D propagator through the expression

$$P_{1D}(x) = \sum_{n=0}^{N-1} a_n \psi_n(u,x), \tag{9}$$

where

$$\begin{aligned} \psi_n(u,x) &= \frac{i^n}{\sqrt{2\pi u}} \phi_n\left(\frac{1}{2\pi u}, x\right) \\ &= \frac{1}{\sqrt{2^{n+1}\pi n! u}} e^{-x^2/(2u^2)} H_n(x/u). \end{aligned} \tag{10}$$

The basis functions $\psi_n(u,x)$ are real-valued, which assures that the probabilities will be real-valued when the a_n are real. This is a consequence of the phase convention we have employed in Eq. (4), which ensures that the real and imaginary parts of the signal are even and odd, respectively. Moreover, Eq. (6) guarantees that the total probability, i.e., the integral of the function $P(x)$ will be unity as expected for a proper probability density function.

Note that the functions $\psi_n(u,x)$, defined in Eq. (10), are the solutions to the eigenvalue equation

$$\left(-u^2 \frac{\partial^2}{\partial x^2} + \frac{x^2}{u^2}\right) \psi_n(u,x) = \lambda_n \psi_n(u,x), \tag{11}$$

with eigenvalues $\lambda_n = (2n+1)$. The SHO analogy emerges because of this equation. The second term is a parabolic potential consistent with Hooke's law. In this context, the parameter u determines the "stiffness" of the spring, and as such, inversely related to the spring constant in the displacement domain. From a practical point of view, the choice of u should be consistent with the signal decay rate for the rapid convergence of the series. Therefore, a reasonable choice of u is the root mean squared displacements of the molecules, i.e.,

$$u = \sqrt{2Dt_d}, \tag{12}$$

where D is the diffusion coefficient and t_d is the diffusion time. With this choice, the first term of Eq. (5) becomes the Stejskal–Tanner formula, where all higher order terms quantify the deviation from a monoexponential decay. Similarly, the first term is a Gaussian in the displacement domain. The crucial point is that all higher order correction terms are orthogonal to this Gaussian term and because the basis is complete, it can successfully approximate any kind of signal decay.

Having an analytical representation of the full q-space data enables one to quantify various features of the reconstructed propagator directly from the a_n coefficients through analytical expressions. Such expressions for the moments of the propagator as well as for the zero net displacement probability are provided in (Özarslan et al., 2011, 2012) and will not be reproduced here for brevity. For applications such as image registration and segmentation, one needs a (dis)similarity measure between different signal or displacement profiles; such a measure will be crucial in the development of scalar indices in the next section. Since the SHORE framework represents the displacement profile as a series of orthogonal functions, the coefficients can be envisioned as components of a vector in a Hilbert space. Therefore, it is meaningful to consider the inner product of two displacement profiles $P(x)$ and $Q(x)$, as

$$\langle P(x), Q(x) \rangle = \int_{-\infty}^{\infty} P(x) Q(x) \; dx. \tag{13}$$

It should be noted that the above quantity can be evaluated in q-space as well. If $E(q)$ and $F(q)$ are, respectively, the signal attenuation profiles corresponding to $P(x)$ and $Q(x)$, then $< P(x), Q(x) >$ is just twice the integral of the real part of the quantity $E^*(q)F(q)$ over the positive q-axis.

If the 1D-SHORE coefficients of $P(x)$ and $Q(x)$, obtained with the scale parameters u and v, are denoted by a_n and b_n, respectively, this inner product is given by

$$\langle P(x), Q(x) \rangle = \sum_{m=0}^{N-1} \sum_{n=0}^{N-1} a_m b_n T_{mn}(u,v), \tag{14}$$

$$T_{mn}(u,v) = \frac{K_{m+n}\sqrt{m!n!}}{\sqrt{2\pi}uv} \sum_{r=0,2,\ldots}^{m} \sum_{s=0,2,\ldots}^{n} \left(\frac{1}{u^2} + \frac{1}{v^2}\right)^{-(m+n-r-s+1)/2} \tag{15}$$

$$\frac{(-1)^{(r+s)/2} 2^{(m+n-r-s)/2} (m+n-r-s-1)!!}{u^{m-r} v^{n-s} (m-r)!(n-s)!r!!s!!}, \tag{16}$$

and K_{m+n} is unity when $m+n$ is even and vanishes otherwise.

Based on the definition of the inner product in Eq. (13), we propose an angular metric (covariance) between two propagators:

$$\cos\theta_{PQ} = \frac{\langle P(x), Q(x) \rangle}{(\langle P(x), P(x) \rangle \langle Q(x), Q(x) \rangle)^{1/2}}, \tag{17}$$

which represents the similarity of the two propagators. As a special case, if the 1D-SHORE coefficients of $P(x)$ and $Q(x)$ are obtained with the same scale parameter, i.e., $u = v$, the angular similarity is given simply by the expression

$$\cos\theta_{PQ} = \frac{\sum_{n=0}^{N-1} a_n b_n}{\left(\sum_{n=0}^{N-1} a_n^2\right)^{1/2}\left(\sum_{m=0}^{N-1} b_m^2\right)^{1/2}}. \tag{18}$$

By continuing the geometric analogy, this measure can be converted readily to a dissimilarity index $\sin\theta_{PQ} = \sqrt{1-\cos^2\theta_{PQ}}$. Note that this dissimilarity is already scaled between 0 and 1. However, depending on the quantity, one may be interested in rescaling the dissimilarity values so that variations within a certain range can be emphasized to improve the contrast in resulting images. To this end, the family of functions defined by

$$\sigma(t,\epsilon) = \frac{t^{3\epsilon}}{1-3t^{\epsilon}+3t^{2\epsilon}}, \tag{19}$$

can be employed, where t is the quantity being scaled (e.g., $\sin\theta_{PQ}$), and ϵ is a positive-valued shape parameter that determines the range of values to be emphasized by the transformation.

MAP-MRI for the 3D problem: a new generalization of DTI

Our formulation for 3D data follows very closely from the above treatment. There are two versions of the three-dimensional formulation. In the first approach, referred to as 3D-SHORE, the same scale parameter is used in all directions, intrinsically assuming that the spring constant is isotropic. This version can be formulated in Cartesian or spherical coordinates. The formulation with isotropic stiffness was introduced by Özarslan et al. (2009c), while an updated presentation with several corrections and extensions is given in Appendix A. The second version, however, features a more general description involving a tensorial scale parameter, which represents the diffusion process better. We refer to this latter approach as MAP-MRI, which is the subject of this section.

We start by generalizing the differential equation whose solutions form the functional basis, $\Psi_{n_1n_2n_3}$. Eq. (11) becomes

$$\left(-\nabla'^{T}\mathbf{A}'\nabla' + \mathbf{r}'^{T}\mathbf{A}'^{-1}\mathbf{r}'\right)\ \Psi_{n_1n_2n_3}\left(\mathbf{A}',\mathbf{r}'\right) = \Lambda_{n_1n_2n_3}\ \Psi_{n_1n_2n_3}\left(\mathbf{A}',\mathbf{r}'\right). \tag{20}$$

Here, and throughout the article, the $'$ symbols indicate that the vectors and matrices are in the image reference frame, which does not vary from voxel to voxel. $\mathbf{A}'$ is a symmetric, positive-definite, second-order (rank-2) tensor that accounts for the spring's stiffness and coupling, as well as its anisotropy. It proves useful to choose our reference frame such that the tensor $\mathbf{A}'$ is diagonal. Let $\mathbf{R}$ be the orthonormal matrix that diagonalizes $\mathbf{A}'$ such that

$$\mathbf{A} = \mathbf{R}\mathbf{A}'\mathbf{R}^{T} = \begin{pmatrix} u_x^2 & 0 & 0 \\ 0 & u_y^2 & 0 \\ 0 & 0 & u_z^2 \end{pmatrix}. \tag{21}$$

Thus, $\mathbf{q}'$ and $\mathbf{r}'$ vectors in the image frame can be transformed into this "anatomical" reference frame through the expressions $\mathbf{q} = \mathbf{R}\mathbf{q}'$ and $\mathbf{r} = \mathbf{R}\mathbf{r}'$, respectively. Note that this reference frame is useful because Eq. (20) becomes separable, and the eigenfunctions are given as the product of three one-dimensional eigenfunctions, i.e.,

$$\Psi_{n_1n_2n_3}(\mathbf{A},\mathbf{r}) = \psi_{n_1}(u_x,x)\psi_{n_2}\left(u_y,y\right)\psi_{n_3}(u_z,z). \tag{22}$$

The eigenvalue corresponding to the above eigenfunction is $\Lambda = 2N + 3$, where $N = n_1 + n_2 + n_3$ defines the total energy of the spring. In a similar fashion, the basis functions in q-space are separable, and given by

$$\Phi_{n_1n_2n_3}(\mathbf{A},\mathbf{q}) = \phi_{n_1}(u_x,q_x)\phi_{n_2}\left(u_y,q_y\right)\phi_{n_3}(u_z,q_z), \tag{23}$$

and the three-dimensional q-space signal can be expressed as

$$S(\mathbf{q}) = \sum_{N=0}^{N_{\max}} \sum_{\{n_1,n_2,n_3\}} \tilde{a}_{n_1n_2n_3}\Phi_{n_1n_2n_3}(\mathbf{A},\mathbf{q}), \tag{24}$$

where the second summation is taken over all possibilities of non-negative indices n_i ($i = 1, 2, 3$), satisfying the condition $n_1 + n_2 + n_3 = N$. The signal attenuation is given by

$$E(\mathbf{q}) = \sum_{N=0}^{N_{\max}} \sum_{\{n_1,n_2,n_3\}} a_{n_1n_2n_3}\Phi_{n_1n_2n_3}(\mathbf{A},\mathbf{q}), \tag{25}$$

where $a_{n_1n_2n_3} = \tilde{a}_{n_1n_2n_3}/S_0$ and S_0 is the non-diffusion-weighted signal intensity revealed by setting $\mathbf{q} = \mathbf{0}$ in Eq. (24), yielding the expression

$$S_0 = \sum_{N=0}^{N_{\max}} \sum_{\{n_1,n_2,n_3\}} \tilde{a}_{n_1n_2n_3}B_{n_1n_2n_3}, \tag{26}$$

where

$$B_{n_1n_2n_3} = K_{n_1n_2n_3}\frac{(n_1!n_2!n_3!)^{1/2}}{n_1!!n_2!!n_3!!}, \tag{27}$$

and $K_{n_1n_2n_3} = 1$ if n_1, n_2, and n_3 are all even, and $K_{n_1n_2n_3} = 0$ otherwise.

The number of unknown coefficients to be estimated from the fit is

$$M_{gen} = \frac{1}{6}(N_{\max}+1)(N_{\max}+2)(N_{\max}+3). \tag{28}$$

However, when complex data are unavailable or when the propagator is expected to be symmetric, which is the case in the absence of flow, Y-shaped crossings, etc., the coefficients corresponding to odd values of N vanish. In this case, the number of coefficients is given by

$$M_{sym} = \frac{1}{6}(F+1)(F+2)(4F+3), \tag{29}$$

where $F = \lfloor N_{\max}/2 \rfloor$.

The propagator, which is just the three-dimensional inverse Fourier transform of $E(\mathbf{q})$ is similarly given by

$$P(\mathbf{r}) = \sum_{N=0}^{N_{\max}} \sum_{\{n_1,n_2,n_3\}} a_{n_1n_2n_3}\ \Psi_{n_1n_2n_3}(\mathbf{A},\mathbf{r}). \tag{30}$$

Taking $\mathbf{A}$ as the covariance matrix of displacements, i.e., setting (Basser, 2002)

$$\mathbf{A} = 2\mathbf{D}t_d, \tag{31}$$

where $\mathbf{D}$ is the diffusion tensor in the anatomical reference frame, reveals the connection between the MAP-MRI method and DTI. Note that $\Phi_{000}(\mathbf{A},\mathbf{q}) = \exp(-2\pi^2\mathbf{q}^T\mathbf{A}\mathbf{q})$. Therefore, with the choice in Eq. (31), the first term of the series in Eq. (25) is nothing but the signal model employed in DTI. It follows naturally that the first term of the series in Eq. (30) is an oriented Gaussian function. All high order terms are the "orthogonal corrections" to the Gaussian approximation.

In many applications of 3D q-space imaging, one is interested in visualizing the orientational features of the propagator. To this end, one can compute the following integral:

$$I_s\left(\hat{\Omega}\right) = \int_0^\infty P\left(r\hat{\Omega}\right) r^{2+s} dr, \tag{32}$$

where $\hat{\Omega} = \left(\Omega_x, \Omega_y, \Omega_z\right)^T$ is a unit vector. $I_s\left(\hat{\Omega}\right)$ can be considered as the sth order "radial moment" of the propagator. This function is expected to be well-defined for all values of s greater than or equal to -2. Note that $I_0\left(\hat{\Omega}\right)$ is a true orientation distribution function (ODF) as its integral over the surface of the unit sphere is unity. The above quantity can be readily estimated from the expansion coefficients via the expression

$$I_s\left(\hat{\Omega}\right) = \frac{\rho^{3+s}}{\sqrt{2^{2-s}\pi^3|\mathbf{A}|}} \sum_{N=0}^{N_{\max}} \sum_{\{n_1,n_2,n_3\}} a_{n_1n_2n_3} \sqrt{n_1!n_2!n_3!} C_{n_1n_2n_3}\left(\hat{\Omega}\right), \tag{33}$$

where

$$C_{n_1n_2n_3}\left(\hat{\Omega}\right) = \sum_{i=0,2,\ldots}^{n_1} \sum_{j=0,2,\ldots}^{n_2} \sum_{k=0,2,\ldots}^{n_3} (-1)^{(i+j+k)/2} \frac{\Gamma\left(\frac{3+s+N-i-j-k}{2}\right) \alpha^{n_1-i} \beta^{n_2-j} \gamma^{n_3-k}}{(n_1-i)!(n_2-j)!(n_3-k)!i!!j!!k!!}, \tag{34}$$

with

$$\rho = \left[\left(\frac{\Omega_x}{u_x}\right)^2 + \left(\frac{\Omega_y}{u_y}\right)^2 + \left(\frac{\Omega_z}{u_z}\right)^2\right]^{-1/2} \tag{35a}$$

$$\alpha = 2\rho\frac{\Omega_x}{u_x} \tag{35b}$$

$$\beta = 2\rho\frac{\Omega_y}{u_y} \tag{35c}$$

$$\gamma = 2\rho\frac{\Omega_z}{u_z}. \tag{35d}$$

Computing the function $I_s\left(\hat{\Omega}\right)$ for many values of $\hat{\Omega}$ using the above expressions yields the desired orientational profile. Note that this profile should be transformed to the image reference frame prior to visualization by using the expression $\hat{\Omega}' = \mathbf{R}^T\hat{\Omega}$.

Scalar indices for 3D q-space imaging (QSI)

In this section, we shall introduce some indices that could be used to quantify various features of the three-dimensional diffusion process. In each subsection, one of the indices is discussed within the context of three-dimensional q-space imaging. Subsequently, an expression relating the index to the MAP-MRI coefficients is provided for easy estimation of the index.

Return-to-the-origin probability (RTOP), mean compartment volume, and their variants for lower-dimensional diffusion

Zero-displacement probabilities and their relations to microstructure

Perhaps one of the most important quantities to obtain is the probability for molecules to undergo no net displacement between the application of the two diffusion sensitizing gradients. This return-to-the-origin probability (RTOP) is simply given by the value $P(\mathbf{0})$, which, according to Eq. (1), is just the integral of the signal attenuation function over the entire q-space, i.e.,

$$RTOP = \int_{\mathcal{R}^3} E(\mathbf{q}) d\mathbf{q}. \tag{36}$$

To illustrate the significance of RTOP, we shall consider a population of isolated pores and employ the simplifying assumption that the gradients are infinitesimally short. Each compartment in the ensemble may be of arbitrary size, shape, and orientation. Since each pore's contribution to the aggregate signal is proportional to the number of spins within the pore, the measured signal attenuation is given by

$$E(\mathbf{q}) = \frac{\int_0^\infty dV\, V f(V) E(\mathbf{q}, V)}{\int_0^\infty dV\, V f(V)}, \tag{37}$$

where $f(V)$ is the compartment volume distribution and $E(\mathbf{q},V)$ is the signal attenuation for a single pore of volume V. Note that the denominator in the above expression is just the mean compartment volume, which we shall denote as $\langle V\rangle$. Inserting Eq. (37) into Eq. (36), we see that the observed RTOP value is given by

$$RTOP = \langle V\rangle^{-1} \int_0^\infty dV\, V f(V)\, RTOP(V), \tag{38}$$

where RTOP(V) is the RTOP value for a single pore of volume V. When the diffusion time (separation of the diffusion gradients) is long enough for the molecules to traverse the longest end-to-end distance within the pore space, this value is just the reciprocal of V (Özarslan et al., 2009b), i.e., $RTOP(V) = V^{-1}$; this follows from the fact that the propagator is the autocorrelation function of the pore indicator function (Callaghan, 1991), which is constant within the pore space and vanishes elsewhere. Consequently, the integral in the above expression is unity, and the RTOP value is nothing but the reciprocal of the statistical mean pore volume, i.e.,

$$\langle V\rangle = RTOP^{-1}. \tag{39}$$

This is quite an important result as no assumption on the shape or coherence of the compartments is made.

In environments like white-matter wherein the compartments have significant levels of shape anisotropy (Özarslan, 2009), it may be difficult to satisfy the long diffusion time requirement along certain directions, which could lead to inaccuracies in the estimated mean pore volume. Consequently, in such environments, it is beneficial to consider only those directions along which diffusion is restricted (e.g., on the plane perpendicular to the axons). Since restricted diffusion leads to a significant reduction in the apparent diffusion coefficient (ADC), these directions can be associated with lower ADC values. Thus, for the case of coherently organized white-matter, the orientations along which diffusion is most restricted correspond to the plane defined by the eigenvectors of the diffusion or $\mathbf{A}$ tensor associated with their smaller eigenvalues. Therefore, two-dimensional q-space data can be used to estimate a return-to-the-axis probability (RTAP) through the expression

$$RTAP = \int_{\mathcal{R}^2} E(\mathbf{q}_\perp) d\mathbf{q}_\perp, \tag{40}$$

where $\mathbf{q}_\perp$ denotes the $\mathbf{q}$-vector on the sampled plane. Following the same lines as above, it is straightforward to show that this quantity is simply the reciprocal of the mean cross-sectional area ($\langle A\rangle$), or,

$$\langle A\rangle = RTAP^{-1}. \tag{41}$$

Finally, a return-to-the-plane probability (RTPP) can be computed through a one-dimensional integral of the signal when $\mathbf{q}$ is parallel with the fiber orientation, i.e.,

$$RTPP = \int_{\mathcal{R}} E\left(q_{//}\right) dq_{//}, \tag{42}$$

where $q_{//}$ denotes the component of the **q**-vector along the fiber axis. A derivation similar to those for RTOP and RTAP above reveal that for diffusion taking place within coherently oriented capped cylinders, RTPP is equal to the reciprocal of the mean length of the cylinders. However, inside substantially prolate confinements, the long diffusion time condition can be difficult to fulfill along the cylinder's axis. In this case, the RTPP value would be close to $(4\pi D_0 t_d)^{-1/2}$, which is its value for unrestricted diffusion.

Estimation of the zero-displacement probabilities from MAP-MRI coefficients

The MAP-MRI representation of the MR signal enables simple estimation of the RTOP value. The relevant expression is given by

$$RTOP = \frac{1}{\sqrt{8\pi^3|\mathbf{A}|}} \sum_{N=0}^{N_{\max}} \sum_{\{n_1,n_2,n_3\}} (-1)^{N/2} a_{n_1n_2n_3} B_{n_1n_2n_3}. \tag{43}$$

Moreover, since the MAP-MRI coefficients are computed in a reference frame determined by the anatomy, the signal and the propagator can be easily separated into components along the three axes defining the anatomical reference frame. For example, in white-matter areas with coherently oriented fibers, the principal eigenvector of the matrix **A** can be assumed to be the fiber orientation (Basser et al., 1994b), which can be assigned to the x-direction without loss of generality. In this case, RTPP is simply the integral of $P(0, y, z)$ over the yz-plane, while RTAP is equal to the integral of $P(x, 0, 0)$ over the x-axis. In terms of the MAP-MRI coefficients, these quantities are given by

$$RTAP = \frac{1}{2\pi u_y u_z} \sum_{N=0}^{N_{\max}} \sum_{\{n_1,n_2,n_3\}} (-1)^{(n_2+n_3)/2} a_{n_1n_2n_3} B_{n_1n_2n_3} \tag{44a}$$

$$RTPP = \frac{1}{\sqrt{2\pi} u_x} \sum_{N=0}^{N_{\max}} \sum_{\{n_1,n_2,n_3\}} (-1)^{n_1/2} a_{n_1n_2n_3} B_{n_1n_2n_3}. \tag{44b}$$

Measuring the similarity of 3D apparent propagators

In this section, we introduce a similarity measure for two three-dimensional propagators. Our formulation extends the angular metric introduced for the case of one-dimensional propagators. As before, the crucial step involves defining an inner product $(\langle P(\mathbf{r}),Q(\mathbf{r})\rangle)$ of two propagators, $P(\mathbf{r})$ and $Q(\mathbf{r})$, through the three-dimensional version of the integral in Eq. (13). This integral can be evaluated from the MAP-MRI coefficients through the expression

$$(\langle P(\mathbf{r}), Q(\mathbf{r})\rangle) = \sum_{M=0}^{N_{\max}} \sum_{\{m_1,m_2,m_3\}} \sum_{N=0}^{N_{\max}} \sum_{\{n_1,n_2,n_3\}} a_{m_1m_2m_3} b_{n_1n_2n_3} T_{m_1n_1}(u_x, v_x) T_{m_2n_2}\left(u_y, v_y\right) T_{m_3n_3}(u_z, v_z), \tag{45}$$

where $a_{m_1m_2m_3}$ denotes the MAP-MRI coefficient for $P(\mathbf{r})$ obtained with the scale parameters u_x, u_y, and u_z. Similarly, $b_{n_1n_2n_3}$ is the MAP-MRI coefficient for $Q(\mathbf{r})$ obtained with the scale parameters v_x, v_y, and v_z.

An angular metric can be computed via an equation analogous to Eq. (17). When the scale parameters are the same for the two propagators, i.e., $u_x = v_x$, $u_y = v_y$, and $u_z = v_z$, the angular metric can be computed through the simple expression

$$\cos\theta_{PQ} = \frac{\sum_{N=0}^{N_{\max}} \sum_{\{n_1,n_2,n_3\}} a_{n_1n_2n_3} b_{n_1n_2n_3}}{\left(\sum_{M=0}^{N_{\max}} \sum_{\{m_1,m_2,m_3\}} a_{m_1m_2m_3}^2\right)^{1/2} \left(\sum_{N=0}^{N_{\max}} \sum_{\{n_1,n_2,n_3\}} b_{n_1n_2n_3}^2\right)^{1/2}}. \tag{46}$$

It should be noted that the MAP-MRI coefficients are computed in the anatomical reference frame, which varies from voxel to voxel. If the comparisons are to be made in a common reference, e.g., the image or laboratory frame, the coefficients would have to be "rotated" accordingly. This can be done using the well-known transformation rules (Nazmitdinov et al., 1996).

The above expressions are expected to be useful in applications such as image segmentation and registration. They can also be used to compute meaningful indices that quantify various important features of the three-dimensional propagator. Two such indices are introduced next.

Propagator anisotropy (PA)

An important characteristic of the diffusion process is its directional dependence (anisotropy). A scalar index that quantifies the degree of anisotropy is known to be an important marker whose value has been recognized since the early days of DTI (Pierpaoli and Basser, 1996). Indices have been defined for more general high angular resolution acquisitions as well (Özarslan et al., 2005). In this section, we shall move one step further and define an index that relates the entire three-dimensional apparent propagator to a measure of anisotropy. This can be accomplished by computing the angular metric between the propagator, and its isotropic version. The latter can be obtained by computing the isotropic part of the propagator using the scheme detailed in Appendix B. The end result is a series of MAP-MRI coefficients $o_{n_1n_2n_3}$ associated with the isotropic stiffness tensor $\mathbf{A} = u_0^2\mathbf{I}$, where $\mathbf{I}$ is the 3×3 identity matrix. The propagator anisotropy (PA) index then measures the angular similarity between the propagator $P(\mathbf{r})$ and its isotropic part $O(r)$ as introduced in the previous section. We found that rescaling the sine of the angle with the shape parameter, $\epsilon = 0.4$, yields the desired level of contrast in real images. So, we define the PA index through the relationship

$$PA = \sigma(\sin\theta_{PO}, 0.4), \tag{47}$$

where the scaling function $\sigma(.)$ is defined in Eq. (19). Note that the isotropic propagator is rotationally invariant by definition. Therefore, the angular metric can be computed without transforming the coefficients to a common reference frame.

To make comparisons with DTI-based anisotropy information possible, we devise a new DTI anisotropy measure based on the same idea of comparing the dissimilarity of the anisotropic Gaussian propagator to its isotropic version. The corresponding index, which we shall denote by PA_{DTI}, is obtained by using the form for the similarity measure given below:

$$(\cos\theta_{PO})_{DTI}^2 = \frac{8u_0^3 u_x u_y u_z}{(u_x^2+u_0^2)\left(u_y^2+u_0^2\right)(u_z^2+u_0^2)} \tag{48}$$

This similarity measure between the anisotropic Gaussian propagator and the isotropic Gaussian propagator is used for two purposes within the MAP-MRI framework. Its first application involves the determination of u_0 from u_x, u_y, and u_z. Among all choices for u_0 corresponding to different instances of the isotropic propagator, we are interested in the one most similar to our anisotropic propagator characterized by the parameters u_x, u_y, and u_z. Thus, we take the derivative of the above quantity with respect to u_0 and set the result to 0. With the definitions $X = u_x^2$, $Y = u_y^2$, $Z = u_z^2$, and $U = u_0^2$, the value of U that determines the most similar isotropic propagator is given by the root of the cubic polynomial

$$3XYZ + (XY + XZ + YZ)U - (X + Y + Z)U^2 - 3U^3 = 0. \tag{49}$$

This equation has only one real positive root, which determines the value of u_0 for which the similarity measure given by Eq. (48) is maximized.

The second application of Eq. (48) is in the computation of the PA_{DTI} index. After u_0 is determined according to the procedure in the above paragraph, $(\sin\theta_{PO})_{DTI}$ is computed from the resulting maximum value of $(\cos\theta_{PO})^2_{DTI}$, which is subsequently plugged into Eq. (47) to obtain PA_{DTI}.

Since the quantities u_x, u_y, u_z, and u_0 are related to the eigenvalues of the diffusion tensor, PA_{DTI} and traditional DTI-based anisotropy indices like fractional anisotropy (FA) can be written as functions of the same quantities. Note that PA_{DTI} could capture information that is unavailable in more traditional measures of anisotropy like FA. The novel conceptual features of the PA_{DTI} index are the employed angular metric and the notion of the "most similar isotropic propagator" consistent with this metric. On the other hand, traditional DTI indices tend to be based on the statistical spread of the three eigenvalues, which intrinsically assumes that the "most similar isotropic propagator" is defined by the mean of the three eigenvalues of the diffusion tensor. Most importantly for our purposes, the same notion of distance between propagators is employed in the definitions of PA and PA_{DTI}; this feature makes PA_{DTI} useful for comparisons.

Non-Gaussianity (NG)

A similar idea is used to formulate an index of non-Gaussianity that quantifies the dissimilarity between the propagator, $P(\mathbf{r})$, and its Gaussian part, $G(\mathbf{r})$. The latter Gaussian propagator is readily available from a diffusion tensor analysis, and is given solely by the first term of the series in Eq. (30). If the coefficients for the non-Gaussian propagator are computed with the same **A** tensor as in Eq. (31), the similarity between $P(\mathbf{r})$ and $G(\mathbf{r})$ is given by

$$\cos\theta_{PG} = \frac{a_{000}}{\left(\sum_{N=0}^{N_{\max}}\sum_{\{n_1,n_2,n_3\}} a^2_{n_1n_2n_3}\right)^{1/2}}. \tag{50}$$

The non-Gaussianity (NG) index is then defined to be

$$NG = \sin\theta_{PG}. \tag{51}$$

Note that the anatomical reference frame is established by the same tensor, **A**. Thus, there is no need to transform the coefficients into a common reference frame in this case either.

The NG index can be considered an alternative to the kurtosis measure (Jensen et al., 2005), which is referred to as another index for non-Gaussianity. While kurtosis is based solely on the moments of the propagator up to order 4, NG is based on the distance between the entire propagator and its Gaussian counterpart; as such, NG is typically influenced by the propagator's higher order moments. It should be noted that the MAP-MRI coefficients can be employed to accurately estimate all moments of the MAP. In fact, an explicit relationship was provided for the 1D problem elsewhere (Özarslan et al., 2008a) and the temporal scaling of the moments were characterized as a potentially novel contrast by Özarslan et al. (2012). The corresponding expressions for the 3D problem, which could be employed to compute the multivariate kurtosis, were not included here for brevity.

Next, we once again exploit the separability of the MAP-MRI expansion to model diffusion along directions parallel with and perpendicular to the principal eigenvector of the diffusion tensor to quantify the non-Gaussianity of the diffusion process along these directions. We outline how this can be achieved for the orientation along the principal eigenvector, which defines the *x*-axis. We are interested in diffusion along *x*, and thus we set *y* and *z* coordinates to 0. The resulting function has an expansion in the 1D-SHORE basis, and the corresponding coefficients a_{n_1} can be computed by equating the three- and one-dimensional expansions, i.e.,

$$P(x,0,0) = \sum_{N=0}^{N_{\max}}\sum_{\{n_1,n_2,n_3\}} a_{n_1n_2n_3}\psi_{n_1}(u_x,x)\psi_{n_2}\left(u_y,0\right)\psi_{n_3}(u_z,0) \tag{52a}$$

$$= \frac{1}{2\pi u_y u_z}\sum_{N=0}^{N_{\max}}\sum_{\{n_1,n_2,n_3\}} a_{n_1n_2n_3}(-1)^{(n_2+n_3)/2}K_{n_2}K_{n_3}\frac{\sqrt{n_2!n_3!}}{n_2!!n_3!!}\psi_{n_1}(u_x,x) \tag{52b}$$

$$= \frac{1}{2\pi u_y u_z}\sum_{n_1}^{N_{\max}} a_{n_1}\psi_{n_1}(u_x,x), \tag{52c}$$

resulting in the relationship

$$a_{n_1} = \sum_{N=0}^{N_{\max}}\sum_{\{n_2,n_3\}} a_{n_1n_2n_3}(-1)^{(n_2+n_3)/2}K_{n_2}K_{n_3}\frac{\sqrt{n_2!n_3!}}{n_2!!n_3!!}, \tag{53}$$

where the second summation assigns all values of n_2 and n_3 satisfying the condition $n_2 + n_3 = N\text{-}n_1$. These a_{n_1} coefficients can be subsequently used to compute the angular metric between the Gaussian and non-Gaussian propagators along the principal eigenvector: $\cos\theta_{PG//} = a_0\left(\sum_{n_1=0}^{N_{\max}} a^2_{n_1}\right)^{-1/2}$, and $NG_{//} = \sin\theta_{PG//}$ in analogy with Eq. (51).

The derivation for diffusion on the transverse plane follows similarly from the expansions of $P(0, y, z)$, and is based on the expression $NG_{\perp} = \sin\theta_{PG\perp}$ with $\cos\theta_{PG\perp} = a_{00}\left(\sum_{n_2=0}^{N_{\max}}\sum_{n_3=0}^{N_{\max}} a^2_{n_2n_3}\right)^{-1/2}$, where the coefficients $a_{n_2n_3}$ can be computed through

$$a_{n_2n_3} = \sum_{N=n_2+n_3}^{N_{\max}}\sum_{n_1=0}^{N_{\max}-n_2-n_3} a_{n_1n_2n_3}(-1)^{n_1/2}K_{n_1}\frac{\sqrt{n_1!}}{n_1!!}. \tag{54}$$

Methods

Numerical implementation

The actual implementation of the MAP-MRI framework is relatively straightforward. Our implementation consists of the following steps:

1. The MR data set was first used to fit the equation $S(\mathbf{q}') = S_0\exp\left(-2\pi^2\mathbf{q}'^T\mathbf{A}'\mathbf{q}'\right)$. It is important to impose a positive-definiteness constraint for the tensor $\mathbf{A}'$. To this end, a scheme discussed in Koay et al. (2006) is used. This scheme employs the following steps: (i) By taking the logarithm of both sides of the above equation, one obtains a linear relationship. This equation is solved using a weighted linear regression method. Weighting the logarithm of the signal values by multiplying them with the actual signal values was necessary to reduce the noise-induced effects in the linear estimation (Basser et al., 1994a). (ii) The resulting estimate for the tensor is fed into a modified Cholesky decomposition routine, which is used in obtaining an upper triangular matrix, **U**, so that $\mathbf{U}^T\mathbf{U}$ is as close as possible to the estimate from the weighted linear fit. (iii) The components of the matrix **U** are fed into a Levenberg–Marquardt nonlinear fitting procedure called MPFIT (provided at http://www.physics.wisc.edu/ craigm/idl/fitting.html), to fit the equation $S(\mathbf{q}') = S_0\exp\left(-2\pi^2\mathbf{q}'^T\mathbf{U}^T\mathbf{U}\mathbf{q}'\right)$ to the signal values. The final estimate of $\mathbf{A}'$ is obtained via the expression $\mathbf{A}' = \mathbf{U}^T\mathbf{U}$. We note that any other tensor estimation scheme imposing a positive definiteness constraint could be used for this step.
2. The matrix $\mathbf{A}'$ obtained from the first step is diagonalized. The resulting eigenvalues are assigned to the scale parameters, u_x^2, u_y^2,

and u_z^2. The matrix whose columns are the eigenvectors of $\mathbf{A}'$ is defined to be the transformation matrix $\mathbf{R}$ so that the matrix $\mathbf{A} = \mathbf{R}\mathbf{A}'\mathbf{R}^T$ is diagonal. The $\mathbf{q}'$ vectors were also transformed according to $\mathbf{q} = \mathbf{R}\mathbf{q}'$.

3. This step involves the estimation of the MAP-MRI coefficients from the signal values. The essential goal is to find the set of coefficients that best represents the data (in q-space) while enforcing constraints in the displacement domain (r-space). So, there is only one unified estimation problem, and this set of $a_{n_1n_2n_3}$ coefficients is used in all subsequent computations. First, we discuss how the problem is posed within a quadratic programming framework, and then describe how the constraints on the probability values implied by the coefficients can be imposed.
Posing the estimation problem. Eq. (24) was used to estimate the coefficients $\tilde{a}_{n_1n_2n_3}$ from the entire q-space data consisting of N_{data} points. $N_{\max}$ was taken to be 6 (unless stated otherwise), resulting in $M_{\text{sym}} = 50$ coefficients. The coefficients were cast into an M_{sym}-dimensional vector $\mathbf{a}$, and the signal values were also placed inside a vector of dimension N_{data} denoted by $\mathbf{y}$. The $N_{\text{data}} \times M_{\text{sym}}$ dimensional design matrix $\mathbf{Q}$ was formed by computing the basis functions $\Phi_{n_1n_2n_3}(\mathbf{A}, \mathbf{q})$ in a consistent manner. With these definitions, Eq. (24) turns into a matrix equation $\mathbf{y} = \mathbf{Q}\mathbf{a}$. Thus, we are interested in minimizing the quantity $\|\mathbf{y} - \mathbf{Q}\mathbf{a}\|^2 = \mathbf{a}^T\mathbf{Q}^T\mathbf{Q}\mathbf{a} - 2\mathbf{y}^T\mathbf{Q}\mathbf{a} + \mathbf{y}^T\mathbf{y}$ subject to non-negativity and normalization constraints as described below. It is clear that the estimation of $\mathbf{a}$ can be cast as a convex quadratic programming problem. To solve it, we used the QUADPROG routine in the IMSL library (Rogue Wave Software, Boulder, CO, USA) provided by IDL's (Exelis, Boulder, CO, USA) Advanced Math and Stats Module. This procedure allows the incorporation of constraints in the estimation. This feature was exploited to enforce the positive definiteness of the propagator as described next.
Constraining the estimation. To enforce positive-definiteness, the displacement space is sampled by a Cartesian grid of $35 \times 35 \times 18$ points so that the first "slice" of this grid is on the xy-plane, and the remaining data points have positive z coordinates effectively sampling half of the displacement space. The longest distance from the origin we are interested in sampling was taken to be $r_{\max} = \sqrt{10D_0t_d}$, where D_0 is the bulk diffusivity. Therefore, the spacing between adjacent points was $\Delta_x = r_{\max}/17$. Those points that are farther than $r_{\max}$ from the origin were excluded, resulting in a total of $N_{\text{sample}} = 10{,}690$ samples in the displacement space. Eq. (30) was also turned into a matrix equation using these points for the displacement. The constraints were set up such that the probability density value at each point on this lattice is nonnegative. An additional constraint was imposed by limiting the integral of the probability density (over the sampled half-space) to values less than or equal to 0.5 so that the total number of constraints is $N_{\text{sample}} + 1$. This integral probability value was estimated by adding up the probability density values over the sampled lattice after halving the values that lie on the xy-plane.
In mathematical terms, the constraints can be expressed by the inequality

$$\begin{pmatrix} \mathbf{K} \\ \mathbf{w}^T\mathbf{K} \end{pmatrix}\mathbf{a} \geq \begin{pmatrix} 0 \\ \vdots \\ 0 \\ -0.5 \end{pmatrix}, \tag{55}$$

where $\mathbf{K}$ is an $N_{\text{sample}} \times M_{\text{sym}}$ matrix. The ith row of this matrix, where $1 \leq i \leq N_{\text{sample}}$, is evaluated by computing the function $\Psi_{n_1n_2n_3}(\mathbf{A}, \mathbf{r}_i)$, and multiplying it by $(\Delta x)^3$ for proper scaling. Here, $\mathbf{r}_i$ is the ith sample in the displacement space. The last row is necessary to impose the constraint on the integral of the probability. Here, $\mathbf{w}$ is a vector of N_{sample} elements, indicating the weights of all samples, i.e., the elements of $\mathbf{w}$ take the values of -0.5 and -1 for samples that are on the xy-plane and otherwise, respectively. The minus signs on the elements of $\mathbf{w}$ as well as on the right-hand side of the above matrix inequality are necessary because the constraints define the minimum values whereas the integral probability is bounded from above.
The end result of this step includes the $a_{n_1n_2n_3}$ coefficients, which are obtained by dividing the $\tilde{a}_{n_1n_2n_3}$ estimates by S_0 obtained from Eq. (26) for each voxel of the image. We note that although our implementation is based on quadratic programming, any other constrained optimization framework such as the nonnegative least squares (NNLS) algorithm (Lawson and Hanson, 1987) could be used to estimate the MAP-MRI coefficients.
4. The estimated coefficients were fed into Eqs. (43) and (44a), (44b) to compute the zero displacement probabilities, and into Eq. (51) for the NG indices, respectively. The coefficients were also used in Eq. (33) to visualize the orientational profile $I_s\left(\hat{\Omega}\right)$. Prior to visualization, the transformation $\hat{\Omega}' = \mathbf{R}^T\hat{\Omega}$ was applied to undo the coordinate transformation in Step 2 above.
5. To compute the PA index, essentially the same scheme described in Step 3 was repeated, this time for the formulation in spherical coordinates presented in Appendix A yielding the coefficients κ_{jlm}. In this analysis, the isotropic scale parameter u_0 was taken by finding the roots of the cubic polynomial in Eq. (49) numerically. These κ_{jlm} coefficients were used in computing the MAP-MRI coefficients, $o_{n_1n_2n_3}$, representing the isotropic part of the three-dimensional propagator through Eq. (65). These were further used in the computation of PA (through Eq. (47)) as discussed in the previous section.

All computations above except the computation and visualization of the $I_s\left(\hat{\Omega}\right)$ profiles took 32 min (approximately one minute for the DTI estimation, 10 min for the computation of the MAP-MRI coefficients and zero displacement and non-Gaussianity indices, and another 21 min for the estimation of the coefficients for the isotropic distribution and the PA index) for the slice shown in Fig. 1. The computations were performed on a laptop computer with a 2.6-GHz Core i7 processor (Intel, Santa Clara, CA, USA) using the IDL programming language (Exelis, Boulder, CO, USA). Significant improvements in computational speed can be achieved via more efficient implementations, through parallelization, and low-level programming languages.

MR image acquisition

MR images of an excised, formalin-fixed marmoset brain washed in buffered saline were acquired on a 7-T vertical-bore Bruker Avance III scanner (Bruker BioSpin, Billerica, MA, USA) equipped with a micro2.5 gradient system with GREAT 60 amplifiers. The brain specimen was immersed in perfluoropolyether (Fomblin LC/8, Solvay Solexis, Italy), and imaged in a 25 mm NMR tube using a radiofrequency coil with 30 mm diameter. The tube was suspended from the top to avoid contact with the gradient coil. The temperature was monitored during the acquisition.

A diffusion-weighted multislice spin echo EPI pulse sequence with 4 segments was used. A total of 489 acquisitions were performed by sampling q-space on 7 different shells defined by b-values: 200, 800, 1800, 3200, 5000, 7200, and 9800 s/mm^2 obtained by employing gradients of magnitude 109, 218, 327, 436, 546, 655, and 764 mT/m, respectively. The numbers of images acquired on these shells were, respectively, 5, 14, 32, 56, 87, 125, and 170. The gradient vectors on each shell were distributed isotropically over the surface of the respective sphere. MR imaging parameters were: TE = 45 ms, TR = 6 s, Δ = 30 ms, δ = 3 ms, bandwidth = 250 kHz, NEX = 40, matrix = 90×90, number of 2D slices = 20, voxel size = $300 \times 300 \times 600$ μm^3. The acquisition of the entire data set took 5.5 days. Fig. 1 illustrates seven randomly selected images each at a different diffusion-weighting.

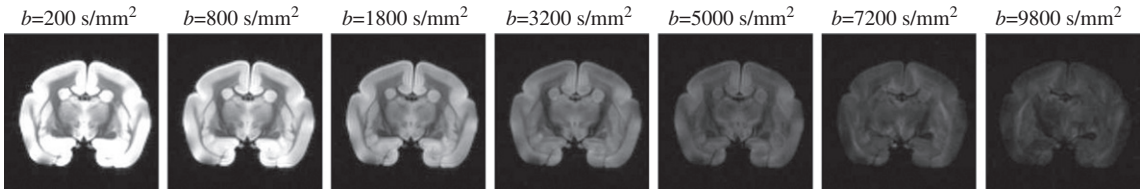

Fig. 1. Sample coronal images for 7 increasing diffusion weightings ($\Delta/\delta = 30/3$ ms) collected from an excised, formalin-fixed marmoset brain (image plane approximately 1.8-mm anterior to bregma (Palazzi and Bordier, 2008)).

Results

Resolution of orientational complexity

In Fig. 2, coronal grayscale PA maps of the excised marmoset brain located 0.7 mm posterior (top row), 1.2 mm anterior (middle row) and 4.9 mm anterior (bottom row) to bregma (Palazzi and Bordier, 2008) are shown with companion MAP-MRI-derived $I_2\left(\hat{\Omega}\right)$ profiles visualized via color glyphs from selected regions. In the top row, there is a diagonal area of crossing between the inferior-located external medullary lamina and the superiorly-located internal capsule within the thalamic reticular nucleus. In the second row, the internal capsule extends superiorly from the bottom left corner through the orthogonal fibers of the external capsule to become the corona radiata. In the bottom row, significant anisotropy is detected in a caudatolenticular gray matter bridge traversing the oblique caudocranial orientation of the internal capsule.

Scalar indices

The scalar MAP-MRI indices introduced above along with the traditional DTI-derived indices (Basser and Pierpaoli, 1996) of S_0, fractional anisotropy (FA), mean diffusivity (MD), diffusivities parallel with ($D_{//}$) and perpendicular to ($D_{\perp}$) the principal eigenvector of the diffusion tensor, and direction-encoded color (DEC) (Pajevic and Pierpaoli, 1999) maps are shown in Fig. 3. In the third row, the MAP-MRI maps of zero displacement probabilities are illustrated. To generate images with consistent dimensions of reciprocal length, the

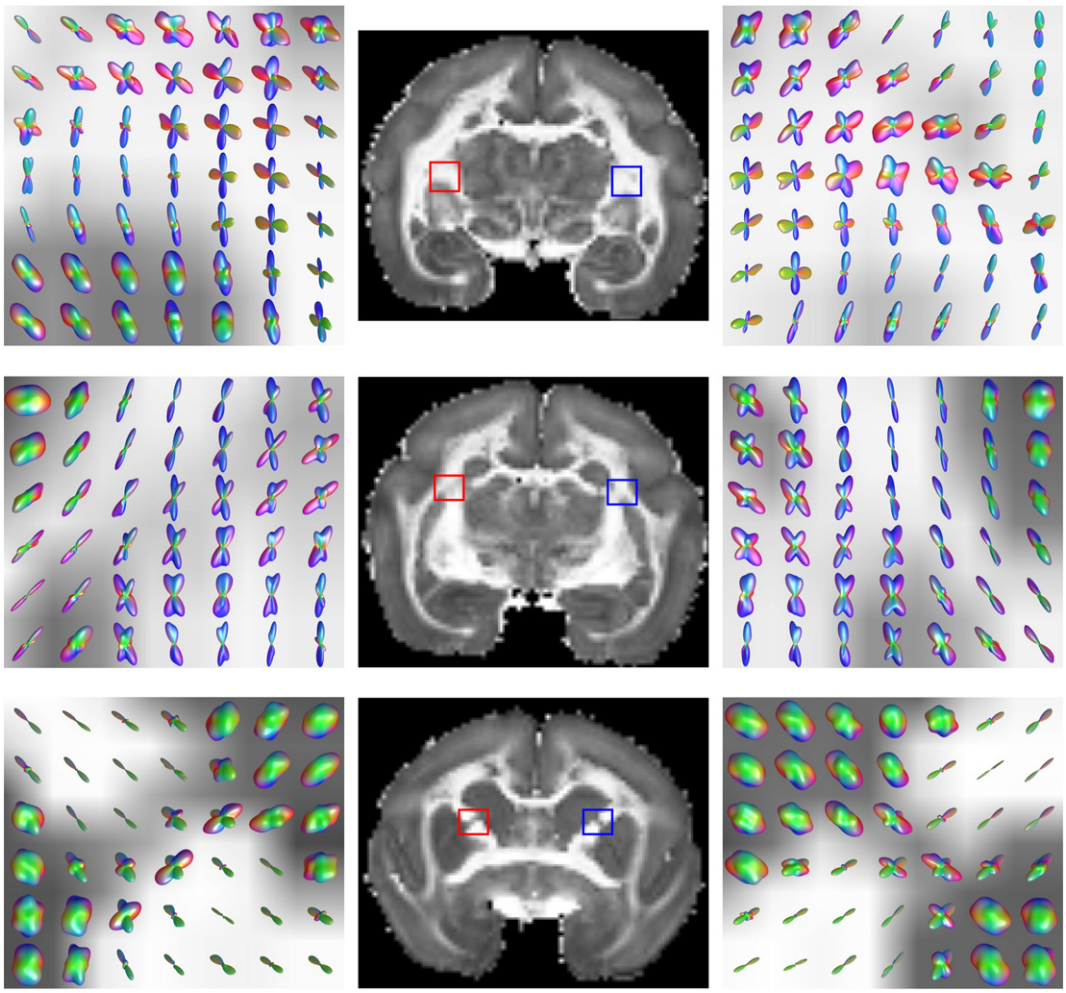

Fig. 2. Resolution of orientational complexity in three different slices (top to bottom) of the marmoset brain. Several regions of interest with orientational heterogeneity are indicated by rectangular boxes in the grayscale PA maps (middle). The $I_2\left(\hat{\Omega}\right)$ profiles visualized via color glyphs (right and left) illustrate the distinct fiber orientations resolved by the MAP-MRI technique.

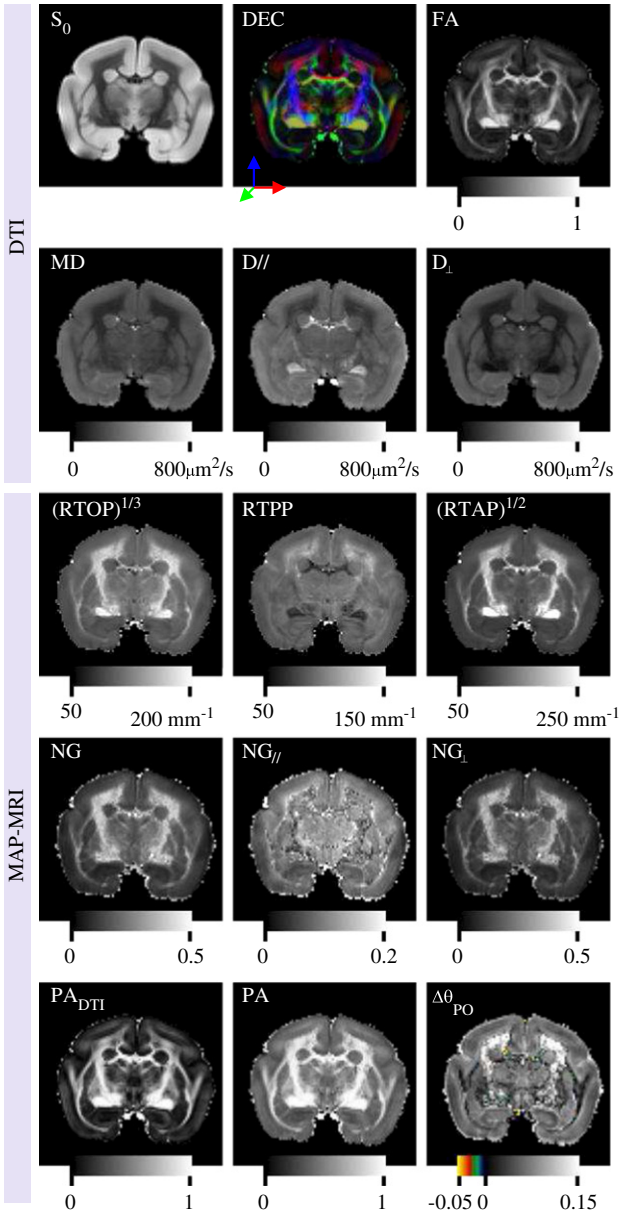

Fig. 3. Traditional DTI and MAP-MRI-derived parameter coronal maps of marmoset brain. First two rows: traditional DTI-derived maps of non-diffusion attenuated signal (S_0), direction encoded color (DEC), fractional anisotropy (FA), mean diffusivity (MD), and diffusivities along ($D_{//}$) and perpendicular ($D_{\perp}$) to the principal eigenvector. Third row: three zero displacement probabilities are shown. The cube-root of the return-to-the-origin probability (RTOP), and the square root of the return-to-the-axis probability (RTAP) are provided so that these quantities have the same dimension with the return-to-the-plane probability (RTPP). Fourth row: three non-Gaussianity indices (from left to right: three-dimensional, parallel with and perpendicular to the principal eigenvector of the diffusion tensor) are illustrated. Fifth row: maps of DTI-derived and MAP-MRI-derived propagator anisotropy (PA) maps are illustrated. The final image depicts the quantity $(\theta_{PO})_{MAP} - (\theta_{PO})_{DTI}$ that represents the difference in the anisotropy maps obtained via MAP-MRI and DTI schemes. Please see the Results section for complete description of the differences between specific conventional DTI and MAP-MRI parameters.

cube root of RTOP and square root of RTAP are shown. There appear to be two main clusters of voxels in the $(RTOP)^{1/3}$ image wherein the white-matter areas generally appear hyperintense, and gray-matter areas make up the lower intensity regions. There is limited contrast within each cluster. The RTPP and RTAP values can be seen as the "decomposition" of the RTOP values into components parallel and perpendicular to the direction of the primary eigenvector of the diffusion tensor, respectively. Since gray-matter areas are relatively isotropic, this decomposition does not change the values significantly—the intensity differences between the three images are mostly due to differences in the scaling of the underlying values. However, in highly anisotropic white-matter areas, RTPP is significantly smaller than $(RTAP)^{1/2}$ as the propagator is considerably broader along the fiber orientation. Interestingly, the RTPP values in white-matter are distributed around the values for gray-matter. There is some contrast within the white-matter areas. The higher intensity regions in the RTPP map are expected to correspond to the white-matter areas with complex fiber orientation distributions (e.g., due to crossing or fanning fibers) or substantial presence of isotropic restrictions (e.g., glial cells). Indeed, a portion of these white-matter regions with larger RTPP values, most notably in corona radiata, exhibit crossing patterns in the orientation maps (not shown). On the other hand, the RTPP values are small in regions with highly anisotropic, coherent single fiber architecture such as the corpus callosum, internal capsule and optic tracts. The principal eigenvector of the diffusion tensor deviates substantially from the fiber orientations in regions with crossing fibers. This deviation does not occur in regions with coherent fiber architecture, which appear hypointense in RTPP maps. Thus, we conclude that the local apparent propagator is considerably broader along the fiber orientation. Similar though inverted features of the contrast in the $D_{//}$ maps support this conclusion. The contrast in the $(RTAP)^{1/2}$ map is similar to that in the $(RTOP)^{1/3}$ image, with the main difference being the enhanced contrast between the coherently organized white-matter areas and gray-matter.

The fourth row of Fig. 3 shows the non-Gaussianity (NG) indices associated with the three-dimensional propagator (left), along the principal eigenvector of the diffusion tensor ($NG_{//}$, middle), and perpendicular to it ($NG_{\perp}$, right). Note the different scaling employed in the $NG_{//}$ map. The contrast in the NG map is very similar to that in the $(RTOP)^{1/3}$ image wherein the white-matter areas similarly exhibit greater overall non-Gaussianity than the gray-matter regions. The decomposition of this non-Gaussianity into directions parallel with and perpendicular to the principal eigenvector of the diffusion tensor, however, yields very different results. The $NG_{//}$ map is relatively homogeneous (despite the narrower dynamic range captured by the scaling); the most significant elevation occurs within voxels of subcortical white matter. Based on their relative locations, these anatomic regions appear to represent an interface between cortex and classic white matter tissue architectures that may be susceptible to partial volume effects. We note that lower S_0 values in white-matter and rapid decay along the fiber orientation could push the signal toward the Rician noise floor at larger q-values, which would lead to an apparent non-monoexponential behavior (Koay et al., 2009a), thus elevate the observed $NG_{//}$ value in white-matter. Nonetheless, the lack of contrast between white- and gray-matter suggests that diffusion is relatively Gaussian throughout gray-matter and parallel to coherent fiber orientations within white-matter. Note that this information and contrast are not available in any of the DTI-derived maps. Non-Gaussianity in the orientation perpendicular to the principal eigenvector is the major contributor to the overall non-Gaussianity; thus the contrasts in NG and $NG_{\perp}$ maps are similar. It is interesting that in all NG maps, fiber crossings in white-matter do not contribute to non-Gaussianity—an assumption previously employed by the multi-tensor models.

Finally, anisotropy measures are shown in the last row of Fig. 3. On the left is the PA_{DTI} index, which is computed from Eqs. (48) and (47) and is based on the distance between the propagator implied by DTI and the Gaussian component of the isotropic distribution, which is most similar to the anisotropic Gaussian propagator as described in Section 4.3. This Gaussian and isotropic distribution is defined by the first term in the MAP-MRI representation of the isotropic propagator as described in Appendix B. Similarly, the map in the middle is the propagator anisotropy (PA) index that is based on the dissimilarity of MAP-MRI's full propagator, and possibly non-Gaussian isotropic

propagator. Finally, the image on the right is the difference between the angular dissimilarities employed in the computation of PA_{DTI} and PA indices. The PA_{DTI} map is very similar to the FA map as expected for all DTI-based anisotropy images. The intensity differences between FA and PA_{DTI} maps are due to the way the indices are defined. The PA_{DTI} index has the advantage that its definition employs the same approach taken in the development of the PA index. To compare the PA map with its DTI version, we used the differences between the angular dissimilarity measures rather than the actual PA values to keep the final difference map insensitive to the employed scaling function. The difference image is scaled such that positive values are represented in grayscale while anisotropy decrease is represented in a color scale (Özarslan et al., 2008b). Anisotropy in the full MAP is significantly greater than the anisotropy of DTI's Gaussian propagator in most voxels, except for a few voxels immediately adjacent to the ventricles or basal cisterns (demonstrated by the color portion of the scale). Interesting contrasts appear within gray- and white-matter regions in the angular difference map. Anisotropy is well-captured by DTI in the corpus callosum, external capsule and temporal subcortical white matter, resulting in hypointense regions in the angular difference map. However, in more paramedian regions like the internal capsule, corona radiata and parietal subcortical white matter, non-Gaussian terms seem to contribute significant levels of anisotropy to the PA measure, thus yielding large $\Delta\theta_{PO}$ values.

Compared to DTI, MAP-MRI's PA indices also detect more underlying structural anisotropy within traditional gray matter structures, such as the cortex, thalamus and caudate nucleus in the coronal slice shown. For example, there is more apparent anisotropy within the deep and superficial layers of the parietal cortex presumably from the pyramidal neuron exiting axons and peripheral dendritic trees, respectively. Similarly, there is increased anisotropy detected throughout the dentate gyrus likely from the radial granule cell neuron orientations. Thus, tractography based on the PA values obtained via MAP-MRI may increase our ability to interrogate neuronal connectivity within nervous tissue structures that do not just contain coherently-oriented macroscopic axon bundles (Shepherd et al., 2006).

The reciprocal of the RTOP and RTAP values have the dimensions of volume and area, and can be used to derive maps of apparent mean volume (AMV) and apparent mean cross sectional area (AMCSA), respectively (Fig. 4). For clarity, only those voxels with a PA_{DTI} value of at least 0.4 are included in the AMCSA maps as the AMCSA parameter is more meaningful in white-matter. Under certain idealized conditions, these parameters then equal the mean volume and mean cross-sectional area of the pores that contain the observed water molecules (see Theory). This suggests that AMV and AMCSA maps may correlate with the volume and cross-sectional area of cells within nervous tissue. Because the myelinated white-matter axons are not very permeable, the influence of axons' cross-sectional area on the computed AMCSA map is expected to be strong. Indeed, Ong et al. (2008) report that zero displacement probabilities are inversely related to the axon diameter in excised mouse spinal cord specimens. In the present marmoset data, the AMCSA values for the corpus callosum are approximately 13 μm^2, which corresponds to about a 2 μm radius if the cross section of the pores is assumed to be perfectly circular. Some overestimation is expected since this analysis does not account for the extracellular space (Ong et al., 2008). Most voxels within the marmoset brain dataset will contain more complex and heterogeneous tissue architectures than simple corpus callosum or spinal cord white matter, but Fig. 4 suggests that cell size distribution is one of the determinants for the computed AMCSA and AMV values. This will require further investigation in future studies.

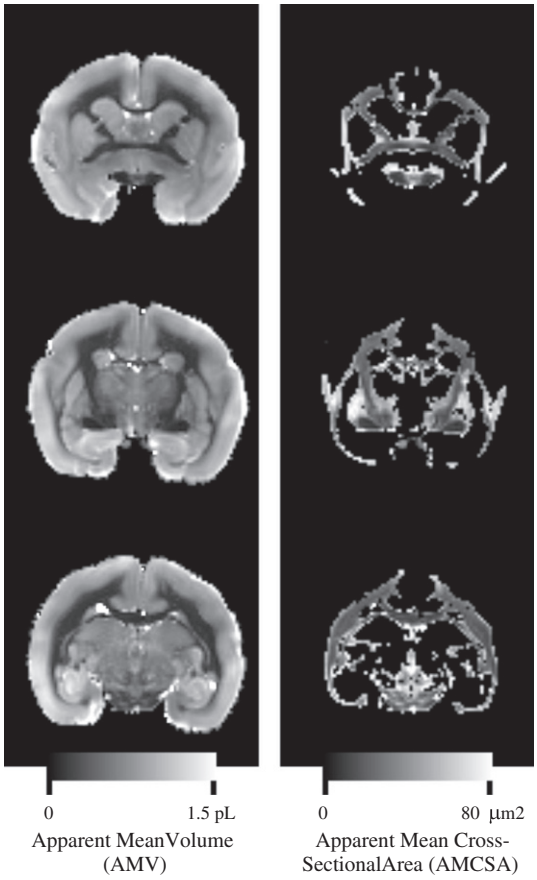

Fig. 4. Apparent mean volume (left) and apparent mean cross-sectional area (right) maps. For clarity, the latter was shown only on white-matter areas determined by including those voxels with a PA_{DTI} value of greater than 0.4. The AMCSA values for the corpus callosum are approximately 13 μm^2, which corresponds to a radius of about 2 μm for pores with perfectly circular cross sections. Each row depicts these images for a different slice in the marmoset data set.

MAP analysis on limited data

The original marmoset brain imaging dataset comprises 489 different images obtained by sampling the q-space up to a b-value of 9800 s/mm^2. This is a relatively time- and gradient-intensive protocol, which would be difficult to acquire when strong gradient coils, large signal-to-noise ratios, and/or long acquisition times are unavailable, which is invariably the case in clinical settings. To assess the feasibility of the method under more clinically-feasible conditions, we repeated the MAP-MRI analysis using a small subset of the entire data set. Specifically, we used the data points up to a b-value of 3200 s/mm^2, and further reduced the total number of q-space samples used in the MAP-MRI analysis by including those points with a non-negative z-component. This resulted in a total of only 55 data points. Fig. 5 illustrates the MAP-MRI results obtained from the full (left) and partial (right) datasets. It was necessary to reduce N_{max} to 4 for the latter. This choice was established on observations of the condition number of the design matrix and simulations performed on well-characterized systems. The estimations are expected to be most meaningful when the condition number of the design matrix is not very large. When we use the full data set, the condition numbers were found to be 18, 250, and 5800 when N_{max} was set to 4, 6, and 8, respectively. When the small subset of the entire data set is used (to generate the right hand side of Fig. 5), the condition numbers are 62 and 2600 for N_{max} values of 4 and 6, respectively. Based on these findings, we have decided to use $N_{max} = 6$ for the full data set, and $N_{max} = 4$ for its subset. Further simulations of idealized systems (results not shown) confirmed that reasonable estimates are achieved with these choices for N_{max}.

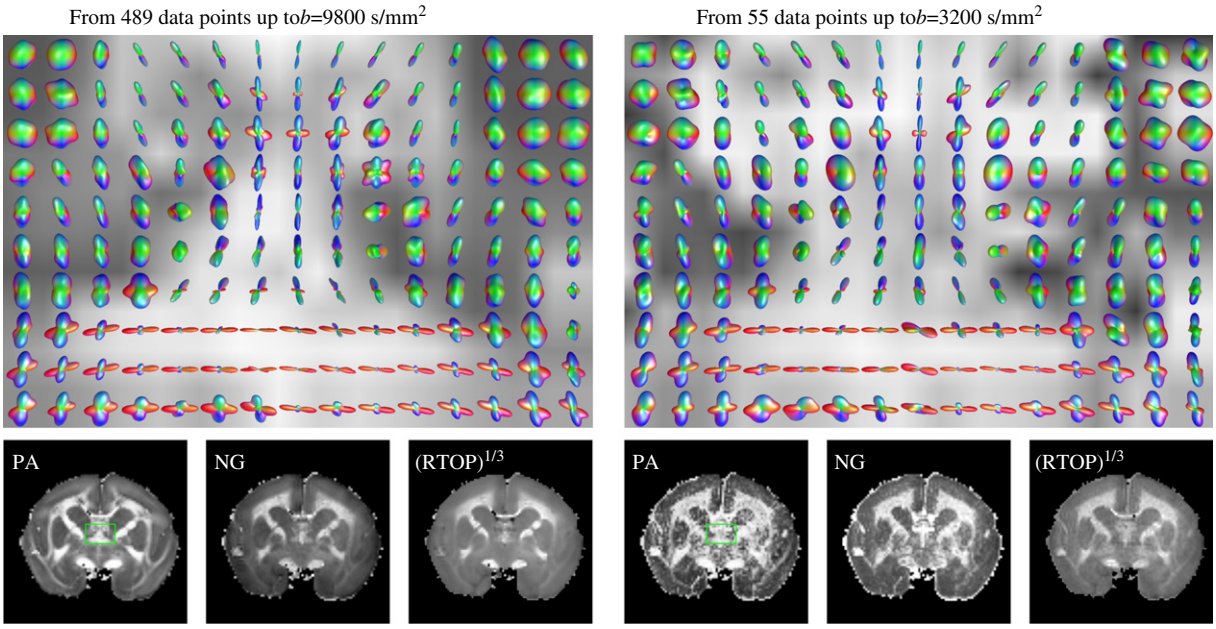

Fig. 5. MAP reconstructions from limited data. MAP-MRI results obtained by using all 489 q-space samples (on seven shells) are shown on the left. A small subset of the dataset comprising 55 samples was obtained by including only those points with a b-value of 3200 s/mm^2 or less that are located in one of the hemispheres. MAP reconstructions and scalar images obtained by using these 55 points are shown on the right.

The orientation profiles, overlaid on the coronal grayscale PA maps, demonstrate the impact of reconstruction with partial data on a region 4.3 mm anterior to bregma (Palazzi and Bordier, 2008) with the anterior commissure (left-to-right) and septal fornix (through plane central part of figure). It is very encouraging that the partial data reconstruction is reasonably similar to the original one despite significant reductions in the number of images and the range of b-values employed. The scalar maps, particularly the PA image, appear to be affected more. Although the images generated from partial data appear less detailed, more anisotropic, and less Gaussian, much of the information content prevails in the significantly less demanding protocol. Future studies will be directed towards developing a feasible dataset for MAP analysis that overcomes the multiple technical limitations of q-space MRI acquisitions in human subjects.

Choice of the radial moment order, s

The maps in Figs. 2 and 5 were generated by computing the integral in Eq. (33) with $s = 2$. Fig. 6 shows the maps as a function of s for three different ROIs representative of white-matter regions with coherent (green box) and crossing (red box) fibers, and cortical gray-matter (blue box). In the last column, glyphs representing the Gaussian propagator associated with the DTI analysis, obtained from the first term of the MAP-MRI representation, are shown. It should be noted that DTI's Gaussian propagator has the same orientational information for all s. Setting it to some "non-special" value like 5 was to emphasize that the derivations would be valid for any value of s. The function $I_0\left(\hat{\Omega}\right)$ is a true orientation distribution function (ODF) as its integral over the sphere is unity. Fig. 6 demonstrates that increasing s leads to sharper orientation profiles. However, at very large s-values, distinct fiber orientations tend to merge and some orientational features start to disappear. Disappearance of orientational complexity was observed in simulations of multifiber systems as well (results not shown) indicating that very large values of s should be avoided. Based on these observations, we argue that the orientational features of the propagator can be captured adequately when s is set to a value slightly above 0—hence our choice $s = 2$ in Figs. 2 and 5.

Orientation profiles in the anatomical reference frame

As described in the Theory section, the reconstruction is performed in the reference frame in which the diffusion tensor is diagonal. When the orientational features of the underlying propagator are to be visualized, the reconstructed MAP needs to be transformed back into the reference frame common to all voxels (the image reference frame). This was accomplished for the function $I_s\left(\hat{\Omega}\right)$ by transforming its argument via the expression $\hat{\Omega}' = \mathbf{R}^T\hat{\Omega}$. This transformation was necessary to provide a correct representation of the glyph consistent with the location of the voxel within the entire image. However, the form of the apparent propagator before it undergoes this transformation could be potentially very useful as well. To illustrate this point, in Fig. 7 we show eight voxels selected within the cortical gray-matter of the marmoset brain. These voxels are marked via blue dots on the PA map on the left. The corresponding set of orientational profiles before and after the reference frame transformation are shown on the right. The approximately radial preference of diffusion within the cortex is evident from the top row, which provides the glyphs after the transformation. On the other hand, the glyphs in the anatomical reference frame, illustrated on the bottom row, are aligned so that the preferred orientation is consistently along the horizontal direction, which follows from assigning the largest eigenvalue of the diffusion tensor to the horizontal axis in the diagonalization scheme. Having the propagator defined in a consistent frame of reference could make it possible to quantitate the parameters associated with the shape of the apparent propagator without having the influence of its orientation. By using a metric between the propagators (e.g., the angular metric employed in the formulation of the scalar indices in this work), the image could be clustered into regions with similar shape characteristics (Freidlin et al., 2007). We envision this approach to be useful in addressing problems such as cortical parcellation.

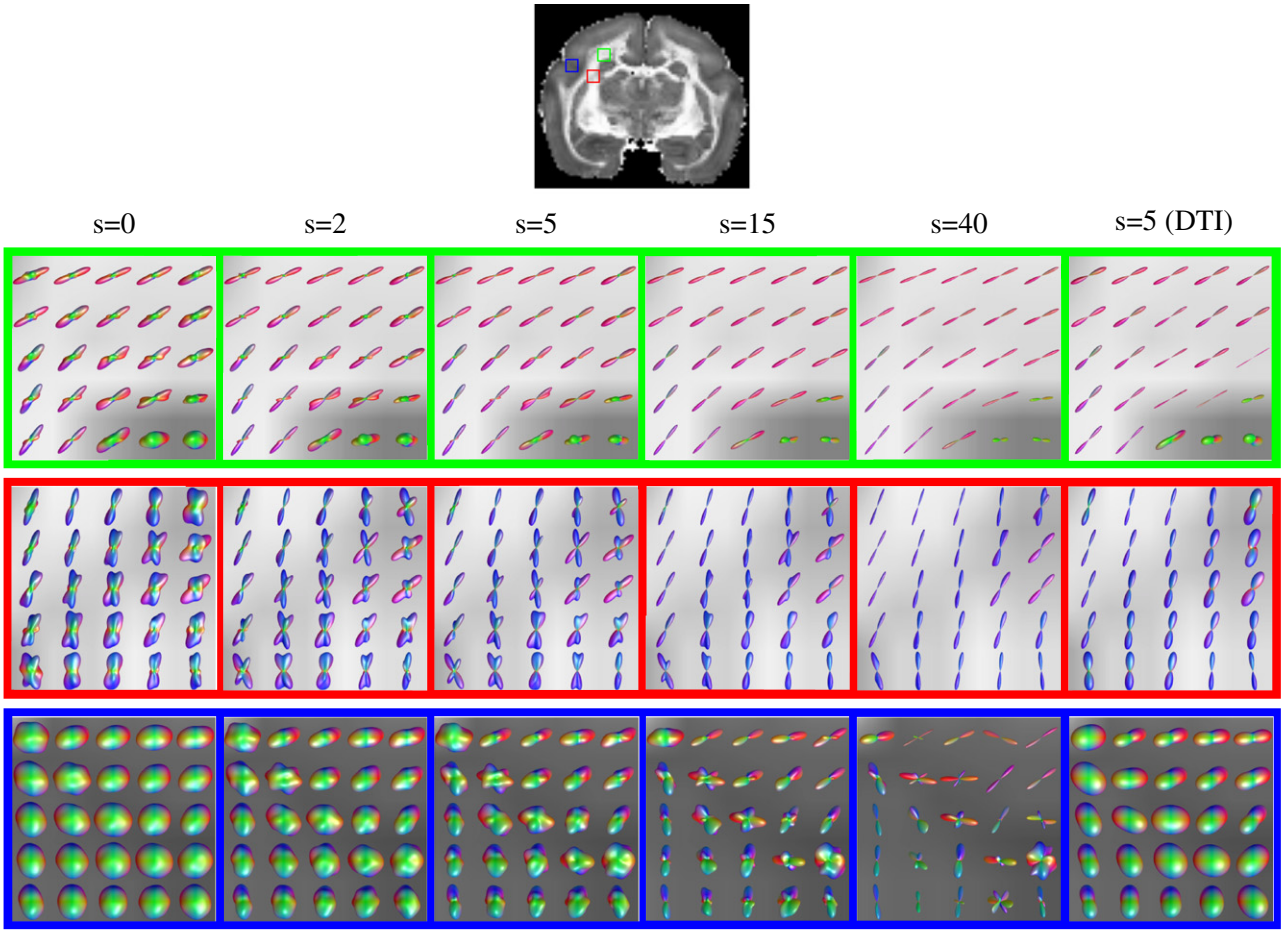

Fig. 6. The effect of the "radial moment", s, on the orientation profiles. The top image shows three ROIs representative of white-matter regions with coherent (green) and crossing (red) fibers, and cortical gray-matter (blue). The glyphs illustrate the corresponding $I_s(\hat{\Omega})$ profiles with different values of s. For comparisons, the last column shows the $I_5(\hat{\Omega})$ profiles obtained from the leading DTI term of the MAP-MRI representation.

Discussion

Influence and estimation of the tensorial scale parameter

The MAP-MRI framework requires the estimation of not only the coefficients $\tilde{a}_{n_1n_2n_3}$ but also the anisotropic scale parameter $\mathbf{A}'$ (hence $\mathbf{A}$) as seen in Eq. (24). A novel aspect of our implementation, which proved to be very robust in practice, involves breaking this otherwise challenging computational problem into two very well-studied problems of (i) positive-definite tensor estimation to obtain $\mathbf{A}'$, and (ii) convex quadratic programming to estimate the coefficients $\tilde{a}_{n_1n_2n_3}$. Although the coefficient estimates depend on $\mathbf{A}'$, we have observed that the propagator and the scalar measures are very weakly dependent on the particular value of $\mathbf{A}'$, which functions merely as a scale parameter. This dependence is weak because the employed basis is complete, and thus capable of representing any function. For this reason, a scale parameter is not even used in statistics literature (see e.g., Schwartz (1967)). However, to efficiently represent the propagator (i.e., with few terms in the series), one needs a scale parameter in reasonable proximity to the width of the functions being used. In an earlier implementation of the method (results not shown), we used only those data points in the low-q regime to estimate the tensor. Although the tensor fit was very satisfactory, the end results were not as good as those we obtained when the tensor model was fitted to the entire data set. This is because when the entire data set is used, the scale parameter captures the overall

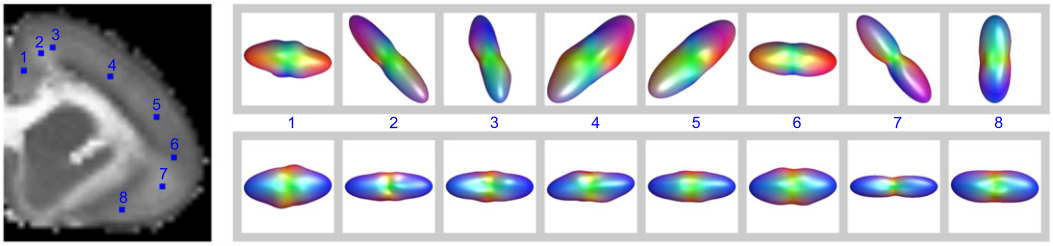

Fig. 7. Eight selected voxels within the cortex of the marmoset brain (left panel) with the corresponding orientation glyphs in image and anatomical reference frames (top & bottom, respectively) associated with each voxel demonstrated to the right.The latter profiles are available from the function $I_s(\hat{\Omega})$ prior to the coordinate transformation $\hat{\Omega}' = \mathbf{R}^T\hat{\Omega}$, and provide the glyphs oriented in a consistent way that could be useful when the orientation-independent features of the propagator need to be compared.

structure of the data set better even though the tensor fitting yields relatively large residuals. These residuals are partly due to the non-Gaussianity of the diffusion process. Thus, they are modeled by the subsequent terms of the MAP-MRI series. It should be noted that an important feature of the tensorial scale parameter is its anisotropy. In certain anatomical regions, decay rates along some directions can be an order of magnitude different than rates along other directions. Therefore, it is important to employ an anisotropic scale parameter; not doing so would lead to employing scale parameters far from its optimal value along some directions. This problem was not realized in some of the earlier works. To assess the quality of the fitting achieved, we computed the adjusted R^2 values for all voxels. These values were clustered very close to unity, with slight reductions in white-matter regions. This behavior can be attributed to the sharpness of the diffusion profiles and the effects of noise (see the S_0 map in Fig. 3). Nonetheless, an average adjusted R^2 value of $0.98 \pm .07$ across the brain parenchyma was observed, demonstrating the level of data fidelity achieved using the basis along with our estimation scheme. Reliance on the tensor model as its first step is a useful feature of our technique also because it makes comparison with DTI meaningful and convenient (see above).

Scalar quantities for diffusion along parallel and perpendicular directions

Yet another novel feature of the MAP-MRI framework is the formulation of the problem in a reference frame determined by the tensorial scale parameter $\mathbf{A}'$. This feature enabled us to introduce scalar measures parallel with and perpendicular to the principal eigenvector of this tensor. By no means do we suggest that this decomposition would consistently represent diffusion parallel with and perpendicular to the fiber orientation as the principal eigenvector of $\mathbf{A}'$ would coincide with the fiber orientation only in regions with highly coherent fiber bundles. The mismatch between the principal eigenvector and the fiber orientation is expected to be most significant in white-matter areas with more than one distinct fiber bundles. Consequently, the presence of fiber crossings is interpreted as one of the determinants of contrast in these scalar maps. In fact, contrast induced by fiber-crossings was observed to some extent in RTPP maps as discussed above.

Comparison with reconstruction via Gram–Charlier series

The MAP-MRI framework has a number of important differences from the reconstruction via the Gram–Charlier series, which also employs Hermite functions, but is based on the cumulant expansion of the characteristic function (Liu et al., 2003, 2004). First, the signal models are different. In the cumulant expansion approach, the logarithm of the signal (the characteristic function) is expanded in a Taylor series, and the cumulants are estimated from the coefficients of this non-orthogonal expansion. As such, the Hermite functions do not appear in the signal domain. Unlike in this approach, our signal model employs the orthogonal basis of Hermite functions (see Eqs. (3) and (24)). The first terms in both approaches contain Gaussians; hence both techniques are generalizations of DTI. However, unlike in the case of cumulant expansion, the tensor that we employ functions as a scale parameter, which is estimated from the entire q-space data. It is not meant to represent the second order cumulants of displacements. There are a number of difficulties associated with applying the Gram–Charlier series to the propagator reconstruction problem. It is well known that the Gram–Charlier series does not yield a proper (e.g., positive-valued) propagator in many cases of interest (Blinnikov and Moessner, 1998; Pawula, 1987). Application of this technique to reconstruct the diffusion propagator has proven to be problematic within the diffusion MR context as well (Ghosh et al., 2010). Another problem is that the cumulant expansions suffer from limited radius of convergence (Frøhlich et al., 2006), and can fail to model the high-q behavior of the signal decay profiles (see Figs. 1 and 5 in Özarslan et al. (2013)). These problems are overcome in the MAP-MRI framework.

Other applications of the method

The developed method can be used as a numerical tool to aid in addressing several important problems that involve the estimation of microstructural parameters. For example, the decomposition of the signal into directions parallel and perpendicular to the fiber direction could make it very convenient to employ the AxCaliber model (Assaf et al., 2008) to determine the axonal size for arbitrarily oriented fibers. Because the MAP-MRI framework enables the estimation of indices such as RTOP that demands a complete characterization of q-space in a robust way, a four-dimensional acquisition (three spatial and one temporal) to characterize the temporal scaling (TS) contrast (Özarslan et al., 2012) could be feasible that would produce meaningful estimates of the apparent fractal dimension in the brain (Özarslan et al., 2006a). The ability of the Hermite functions to represent the three-dimensional q-space signal could be exploited along with the compressed sensing method (Candés et al., 2006; Donoho, 2006) to reconstruct the propagator (Paulsen et al., 2011; Rathi et al., 2011) from sparsely sampled data (Koay et al., 2012) to further boost the efficiency of the MAP-MRI technique. Similar to what was done for one-dimensional q-space imaging (Özarslan et al., 2012), any bias due to the Rician character of the signal, particularly at large b-values could be mitigated in three-dimensional q-space data by incorporating the MAP-MRI framework into a method developed to remove the effects of noise in magnitude-valued data (Koay et al., 2009a,b). The MAP-MRI method could be used with complex data as well; in that case, the odd-ordered $\phi(.)$ and $\psi(.)$ functions would also have to be included in the analysis. This would enable the reconstruction of asymmetric profiles (Ozcan, 2010), which are known to arise in geometries involving Y-shaped crossings (Liu et al., 2003), a nearby surface on one side of the voxel (Özarslan et al., 2008b), and curving fibers (Özarslan et al., 2009a).

Conclusion

MAP-MRI represents a new comprehensive analytical framework to model the three-dimensional q-space signal and transform it into apparent propagators. The key feature of the approach is the anisotropic spring constant or scale parameter. The anisotropically-scaled basis not only improves the ability of MAP-MRI to adapt to very different signal profiles, but can reduce the technique to the widely-employed DTI method if only the first of the basis functions is employed. Consequently, the MAP-MRI technique subsumes DTI while also providing several novel, quantifiable parameters that capture previously obscured intrinsic features of nervous tissue microstructure. The features of the employed basis make the MAP-MRI framework very robust and it may also be adapted to the technical limitations of *in vivo* imaging of clinical patients. Hence, MAP-MRI should prove helpful for investigating a spectrum of important scientific problems regarding the functional organization of normal and pathologic nervous tissue. This may ultimately lead to increased diagnostic accuracy of diffusion-weighted MRI for patients with CNS disease.

Acknowledgments

The authors gratefully acknowledge Drs. John D. Newman and Afonso C. Silva for the marmoset brain specimen and Liz Salak for editing the manuscript. Special thanks to Jian Cheng for pointing out an error in (Özarslan et al., 2009c). Support for this work included funding from: (i) the Intramural Research Program of the Eunice Kennedy Shriver National Institute of Child Health and Human Development (NICHD),

the National Institutes of Health (NIH), and (ii) the Department of Defense in the Center for Neuroscience and Regenerative Medicine (CNRM) and the Henry M. Jackson Foundation (HJF). (iii) CGK was supported in part by NIH grant no. IRCMH090912-01. (iv) EÖ was supported in part by NIH R01MH074794.

Conflict of interest statement

The authors declare no conflicts of interest.

Appendix A. 3D-SHORE: The special case of isotropic stiffness and its representation in spherical coordinates

In this section, we shall treat a special case of the above formulation in which the stiffness tensor **A** is isotropic. In this case all eigenvalues of **A** are equal, and will be denoted by u_0^2. The operator on the left-hand side of Eq. (20) becomes $-u_0^2\nabla^2 + r^2/u_0^2$, and the problem can be stated in q-space using spherical coordinates as

$$\left(-\frac{1}{(2\pi u_0)^2}\nabla_{\mathbf{q}}^2 + (2\pi u_0)^2 q^2\right)\Xi_{jlm}(u_0,\mathbf{q}) = \Lambda_{jlm}\Xi_{jlm}(u_0,\mathbf{q}), \tag{56}$$

where $q = |\mathbf{q}|$,$\Lambda_{jlm} = 2l + 4j - 1$, and the basis functions are given by

$$\Xi_{jlm}(u_0,\mathbf{q}) = \sqrt{4\pi}i^{-l}\left(2\pi^2u_0^2q^2\right)^{l/2}e^{-2\pi^2u_0^2q^2}L_{j-1}^{l+1/2}\left(4\pi^2u_0^2q^2\right)Y_{lm}\left(\hat{\Omega}_q\right), \tag{57}$$

where $L_k^{\alpha}(.)$ is the associated Laguerre polynomial and $Y_{lm}\left(\hat{\Omega}_q\right)$ is the spherical harmonic, which is a function of the gradient vector's orientation described by the unit vector $\hat{\Omega}_q$. Then the MR signal profile can be expanded in this basis

$$S(\mathbf{q}) = \sum_{N=0}^{N_{\max}}\sum_{\{j,l\}}\sum_{m=-l}^{l}\tilde{\kappa}_{jlm}\Xi_{jlm}(u_0,\mathbf{q}), \tag{58}$$

where the second summation is evaluated over all possible values of $j \geq 1$ and $l \geq 0$ satisfying the condition $2j + l = N + 2$. Fig. 8 illustrates the allowed values of N, l, and j when $N_{\max} = 8$. Here, the squares represent the terms corresponding to the even values of l. Those corresponding to odd values of l, depicted by circles, can be neglected when the propagator is symmetric. Note that each point corresponding to a certain l value contributes $2l + 1$ coefficients as the remaining index m takes values between $-l$ and l.

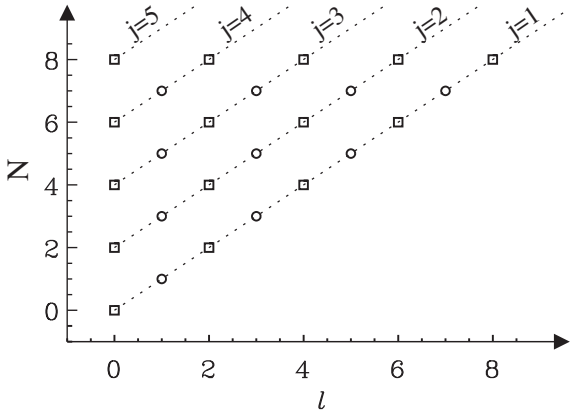

Fig. 8. The values of the indices j, l, and N used for $N_{\max} = 8$ in the representation of the series involving spherical coordinates when the stiffness is isotropic. Each point on this plot represents $2l + 1$ different coefficients as the index m may take any integer value from $-l$ to l. The terms corresponding to odd values of l vanish when the propagator is symmetric, i.e., when the imaginary part of the signal is 0. In this case, the points depicted by circles can be neglected, and the total number of coefficients is reduced from 165 to 95.

Similar to what was done earlier, the MR signal attenuation profile, $E(\mathbf{q})$ can be expanded in the same basis. The coefficients are given by $\kappa_{jlm} = \tilde{\kappa}_{jlm}/S_0$, where

$$S_0 = \sum_{N=0}^{N_{\max}}\tilde{\kappa}_{(1+N/2)00}\frac{(N+1)!!}{N!!}. \tag{59}$$

Since this representation is totally equivalent to the Cartesian representation with isotropic potential (see Pluhar and Tolar (1961)) for the matrix that transforms the $a_{n_1n_2n_3}$ into κ_{jlm} and vice versa), the number of independent coefficients for general propagators is still given by Eq. (28), while for symmetric propagators Eq. (29) holds.

The three-dimensional propagator is expressed by a similar expression

$$P(\mathbf{r}) = \sum_{N=0}^{N_{\max}}\sum_{\{j,l\}}\sum_{m=-l}^{l}\kappa_{jlm}\Upsilon_{jlm}(u_0,\mathbf{r}), \tag{60}$$

where the basis functions are given through a three-dimensional inverse Fourier transform of $\Xi_{jlm}(u_0,\mathbf{q})$ by

$$\Upsilon_{jlm}(u_0,\mathbf{r}) = \frac{(-1)^{j-1}}{\sqrt{2}\pi u_0^3}\left(\frac{r^2}{2u_0^2}\right)^{l/2}e^{-r^2/2u_0^2}L_{j-1}^{l+1/2}\left(\frac{r^2}{u_0^2}\right)Y_{lm}\left(\hat{\Omega}\right). \tag{61}$$

Appendix B. The isotropic propagator and the transition between spherical and Cartesian representations

The spherical representation with the problem featuring isotropic stiffness is most useful within the MAP-MRI framework in obtaining the "isotropic part" of the displacement profile, which is the isotropic displacement profile that most faithfully represents the true, possibly anisotropic, propagator. It is possible to extract the isotropic propagator because the angular dependence is characterized exclusively by the spherical harmonic function, which is separated from the radial dependence of the signal. The isotropic component of the propagator is contained in those terms with $l = m = 0$ only. This condition further implies $j = 1 + N/2$. The relevant basis functions are given by

$$\Upsilon_{(1+N/2)00}(u_0,\mathbf{r}) = \frac{(-1)^{N/2}}{(2\pi)^{3/2}u_0^3}e^{-r^2/(2u_0^2)}L_{N/2}^{1/2}\left(\frac{r^2}{u_0^2}\right). \tag{62}$$

Using the identities (Gradshteyn and Ryzhik, 2000)

$$L_{N/2}^{1/2}\left(\frac{r^2}{u_0^2}\right) = \sum_{\{n_1n_2n_3\}}K_{n_1n_2n_3}L_{n_1/2}^{-1/2}\left(\frac{x^2}{u_0^2}\right)L_{n_2/2}^{-1/2}\left(\frac{y^2}{u_0^2}\right)L_{n_3/2}^{-1/2}\left(\frac{z^2}{u_0^2}\right) \tag{63a}$$

$$L_{n/2}^{-1/2}\left(t^2\right) = \frac{(-1)^{n/2}H_n(t)}{2^n(n/2)!}, \tag{63b}$$

it is straightforward to show that the isotropic propagator is given by

$$P_{iso}(\mathbf{r}) = \sum_{N=0}^{N_{\max}}\kappa_{(1+N/2)00}\sum_{\{n_1,n_2,n_3\}}B_{n_1n_2n_3}\Psi_{n_1n_2n_3}\left(u_0^2\mathbf{I},\mathbf{r}\right), \tag{64}$$

where $\mathbf{I}$ is the 3×3 identity matrix. The above expression is an expansion in the form of the MAP-MRI series, with coefficients

$$o_{n_1n_2n_3} = B_{n_1n_2n_3}\kappa_{(1+N/2)00}. \tag{65}$$

Several inferences can be made from the above findings for isotropic propagators. First, all MAP-MRI coefficients with at least one odd

index vanish. Second, the coefficients with permutations of the indices n_1, n_2, and n_3 are equal to each other. Finally, there are a total of $1 + N_{\max}/2$ unique coefficients that describe an isotropic propagator.

These observations can be used to compute the coefficients for the isotropic, though possibly non-Gaussian, propagator that best describes a given signal profile. To this end, Eq. (58) can be used to estimate $\tilde{\kappa}_{jlm}$, which can be subsequently divided by S_0 to yield κ_{jlm}. The MAP-MRI coefficients describing the isotropic part of the propagator can be obtained by using Eq. (65). Alternatively, one can perform the MAP-MRI fitting with $1 + N_{\max}/2$ unknowns by imposing Eq. (65) from the outset along with $\mathbf{A} = u_0^2\mathbf{I}$.

References

Aganj, I., Lenglet, C., Sapiro, G., Yacoub, E., Ugurbil, K., Harel, N., 2010. Reconstruction of the orientation distribution function in single- and multiple-shell q-ball imaging within constant solid angle. Magn. Reson. Med. 64 (2), 554–566. http://dx.doi.org/10.1002/mrm.22365.

Alexander, D.C., Barker, G.J., Arridge, S.R., 2002. Detection and modeling of non-Gaussian apparent diffusion coefficient profiles in human brain data. Magn. Reson. Med. 48 (2), 331–340.

Anderson, A.W., 2005. Measurement of fiber orientation distributions using high angular resolution diffusion imaging. Magn. Reson. Med. 54 (5), 1194–1206. http://dx.doi.org/10.1002/mrm.20667.

Assaf, Y., Blumenfeld-Katzir, T., Yovel, Y., Basser, P.J., 2008. AxCaliber: a method for measuring axon diameter distribution from diffusion MRI. Magn. Reson. Med. 59 (6), 1347–1354. http://dx.doi.org/10.1002/mrm.21577.

Assemlal, H.-E., Tschumperlé, D., Brun, L., 2009. Efficient and robust computation of PDF features from diffusion MR signal. Med. Image Anal. 13 (5), 715–729. http://dx.doi.org/10.1016/j.media.2009.06.004.

Assemlal, H.-E., Tschumperlé, D., Brun, L., Siddiqi, K., 2011. Recent advances in diffusion MRI modeling: angular and radial reconstruction. Med. Image Anal. 15 (4), 369–396. http://dx.doi.org/10.1016/j.media.2011.02.002.

Basser, P.J., 2002. Relationships between diffusion tensor and q-space MRI. Magn. Reson. Med. 47, 392–397.

Basser, P.J., Pierpaoli, C., 1996. Microstructural and physiological features of tissues elucidated by quantitative diffusion tensor MRI. J. Magn. Reson. B 111 (3), 209–219.

Basser, P.J., Mattiello, J., LeBihan, D., 1994a. Estimation of the effective self-diffusion tensor from the NMR spin echo. J. Magn. Reson. B 103 (3), 247–254.

Basser, P.J., Mattiello, J., LeBihan, D., 1994b. MR diffusion tensor spectroscopy and imaging. Biophys. J. 66 (1), 259–267.

Blinnikov, S., Moessner, R., 1998. Expansions for nearly Gaussian distributions. Astron. Astrophys. Suppl. Ser. 130, 193–205.

Callaghan, P.T., 1991. Principles of Nuclear Magnetic Resonance Microscopy. Clarendon Press, Oxford.

Callaghan, P.T., Eccles, C.D., Xia, Y., 1988. NMR microscopy of dynamic displacements: **k**-space and **q**-space imaging. J. Phys. E 21, 820–822.

Callaghan, P.T., MacGowan, D., Packer, K.J., Zelaya, F.O., 1990. High-resolution *q*-space imaging in porous structures. J. Magn. Reson. 90, 177–182.

Candés, E.J., Romberg, J.K., Tao, T., 2006. Stable signal recovery from incomplete and inaccurate measurements. Commun. Pure Appl. Math. 59, 1207–1223.

Cheng, J., Ghosh, A., Jiang, T., Deriche, R., 2010. Model-free and analytical EAP reconstruction via spherical polar Fourier diffusion MRI. Med. Image Comput. Comput. Assist. Interv. 13 (Pt. 1), 590–597.

Cohen, Y., Assaf, Y., 2002. High b-value q-space analyzed diffusion-weighted MRS and MRI in neuronal tissues — a technical review. NMR Biomed. 15, 516–542.

Cory, D.G., Garroway, A.N., 1990. Measurement of translational displacement probabilities by NMR: an indicator of compartmentation. Magn. Reson. Med. 14 (3), 435–444.

Dell'Acqua, F., Scifo, P., Rizzo, G., Catani, M., Simmons, A., Scotti, G., Fazio, F., 2010. A modified damped Richardson–Lucy algorithm to reduce isotropic background effects in spherical deconvolution. Neuroimage 49 (2), 1446–1458.

Descoteaux, M., Angelino, E., Fitzgibbons, S., Deriche, R., 2007. Regularized, fast, and robust analytical q-ball imaging. Magn. Reson. Med. 58 (3), 497–510. http://dx.doi.org/10.1002/mrm.21277.

Descoteaux, M., Deriche, R., LeBihan, D., Mangin, J.-F., Poupon, C., 2011. Multiple q-shell diffusion propagator imaging. Med. Image Anal. 15 (4), 603–621. http://dx.doi.org/10.1016/j.media.2010.07.001.

Donoho, D.L., 2006. Compressed sensing. IEEE Trans. Inf. Theory 52, 1289–1306.

Frank, L.R., 2002. Characterization of anisotropy in high angular resolution diffusion-weighted MRI. Magn. Reson. Med. 47 (6), 1083–1099.

Freidlin, R.Z., Özarslan, E., Komlosh, M.E., Chang, L.-C., Koay, C.G., Jones, D.K., Basser, P.J., 2007. Parsimonious model selection for tissue segmentation and classification applications: a study using simulated and experimental DTI data. IEEE Trans. Med. Imaging 26 (11), 1576–1584. http://dx.doi.org/10.1109/TMI.2007.907294.

Frøhlich, A.F., Østergaard, L., Kiselev, V.G., 2006. Effect of impermeable boundaries on diffusion-attenuated MR signal. J. Magn. Reson. 179 (2), 223–233. http://dx.doi.org/10.1016/j.jmr.2005.12.005.

Ghosh, A., Özarslan, E., Deriche, R., 2010. Challenges in reconstructing the propagator via a cumulant expansion of the one-dimensional q-space MR signal. Proc Intl Soc Mag Reson Med, vol. 18.

Gradshteyn, I.S., Ryzhik, I.M., 2000. Table of Integrals, Series, and Products, 6th edition. Academic Press, London.

Hess, C.P., Mukherjee, P., Han, E.T., Xu, D., Vigneron, D.B., 2006. Q-ball reconstruction of multimodal fiber orientations using the spherical harmonic basis. Magn. Reson. Med. 56 (1), 104–117. http://dx.doi.org/10.1002/mrm.20931.

Hosseinbor, A.P., Chung, M.K., Wu, Y.-C., Alexander, A.L., 2011. Bessel Fourier orientation reconstruction: an analytical EAP reconstruction using multiple shell acquisitions in diffusion MRI. Med. Image Comput. Comput. Assist. Interv. 14 (Pt. 2), 217–225.

Jensen, J.H., Helpern, J.A., Ramani, A., Lu, H., Kaczynski, K., 2005. Diffusional kurtosis imaging: the quantification of non-Gaussian water diffusion by means of magnetic resonance imaging. Magn. Reson. Med. 53, 1432–1440.

Jian, B., Vemuri, B.C., Özarslan, E., Carney, P.R., Mareci, T.H., 2007. A novel tensor distribution model for the diffusion-weighted MR signal. Neuroimage 37 (1), 164–176. http://dx.doi.org/10.1016/j.neuroimage.2007.03.074.

Kaden, E., Knösche, T.R., Anwander, A., 2007. Parametric spherical deconvolution: inferring anatomical connectivity using diffusion MR imaging. Neuroimage 37 (2), 474–488. http://dx.doi.org/10.1016/j.neuroimage.2007.05.012.

Koay, C.G., Chang, L.-C., Carew, J.D., Pierpaoli, C., Basser, P.J., 2006. A unifying theoretical and algorithmic framework for least squares methods of estimation in diffusion tensor imaging. J. Magn. Reson. 182 (1), 115–125. http://dx.doi.org/10.1016/j.jmr.2006.06.020.

Koay, C.G., Özarslan, E., Basser, P.J., 2009a. A signal transformational framework for breaking the noise floor and its applications in MRI. J. Magn. Reson. 197 (2), 108–119. http://dx.doi.org/10.1016/j.jmr.2008.11.015.

Koay, C.G., Özarslan, E., Pierpaoli, C., 2009b. Probabilistic identification and estimation of noise (PIESNO): a self-consistent approach and its applications in MRI. J. Magn. Reson. 199 (1), 94–103. http://dx.doi.org/10.1016/j.jmr.2009.03.005.

Koay, C.G., Özarslan, E., Johnson, K.M., Meyerand, M.E., 2012. Sparse and optimal acquisition design for diffusion MRI and beyond. Med. Phys. 39 (5), 2499–2511. http://dx.doi.org/10.1118/1.3700166 (May).

Lawson, C.L., Hanson, R.J., 1987. Solving Least Squares Problems. Classics in Applied Mathematics. SIAM, Philadelphia.

Liu, C.L., Bammer, R., Moseley, M.E., 2003. Generalized diffusion tensor imaging (GDTI): a method for characterizing and imaging diffusion anisotropy caused by non-Gaussian diffusion. Isr. J. Chem. 43 (1–2), 145–154.

Liu, C., Bammer, R., Acar, B., Moseley, M.E., 2004. Characterizing non-Gaussian diffusion by using generalized diffusion tensors. Magn. Reson. Med. 51 (5), 924–937 (May).

Nazmitdinov, R.G., Robledo, L.M., Ring, P., Egido, J.L., 1996. Representation of three-dimensional rotations in oscillator basis sets. Nucl. Phys. A 596, 53–66.

Ohanian, H.C., 1990. Principles of Quantum Mechanics. Prentice-Hall, Englewood Cliffs.

Ong, H.H., Wright, A.C., Wehrli, S.L., Souza, A., Schwartz, E.D., Hwang, S.N., Wehrli, F.W., 2008. Indirect measurement of regional axon diameter in excised mouse spinal cord with q-space imaging: simulation and experimental studies. Neuroimage 40 (4), 1619–1632. http://dx.doi.org/10.1016/j.neuroimage.2008.01.017.

Özarslan, E., 2009. Compartment shape anisotropy (CSA) revealed by double pulsed field gradient MR. J. Magn. Reson. 199 (1), 56–67. http://dx.doi.org/10.1016/j.jmr.2009.04.002.

Özarslan, E., Mareci, T.H., 2003. Generalized diffusion tensor imaging and analytical relationships between diffusion tensor imaging and high angular resolution diffusion imaging. Magn. Reson. Med. 50 (5), 955–965. http://dx.doi.org/10.1002/mrm.10596.

Özarslan, E., Vemuri, B.C., Mareci, T.H., 2005. Generalized scalar measures for diffusion MRI using trace, variance, and entropy. Magn. Reson. Med. 53 (4), 866–876. http://dx.doi.org/10.1002/mrm.20411.

Özarslan, E., Basser, P.J., Shepherd, T.M., Thelwall, P.E., Vemuri, B.C., Blackband, S.J., 2006a. Observation of anomalous diffusion in excised tissue by characterizing the diffusion-time dependence of the MR signal. J. Magn. Reson. 183 (2), 315–323. http://dx.doi.org/10.1016/j.jmr.2006.08.009.

Özarslan, E., Shepherd, T.M., Vemuri, B.C., Blackband, S.J., Mareci, T.H., 2006b. Resolution of complex tissue microarchitecture using the diffusion orientation transform (DOT). Neuroimage 31 (3), 1086–1103. http://dx.doi.org/10.1016/j.neuroimage.2006.01.024.

Özarslan, E., Koay, C.G., Basser, P.J., 2008a. Simple harmonic oscillator based estimation and reconstruction for one-dimensional q-space MR. Proc Intl Soc Mag Reson Med, vol. 16, p. 35.

Özarslan, E., Nevo, U., Basser, P.J., 2008b. Anisotropy induced by macroscopic boundaries: surface-normal mapping using diffusion-weighted imaging. Biophys. J. 94 (7), 2809–2818. http://dx.doi.org/10.1529/biophysj.107.124081.

Özarslan, E., Koay, C.G., Basser, P.J., 2009a. Remarks on q-space MR propagator in partially restricted, axially-symmetric, and isotropic environments. Magn. Reson. Imaging 27 (6), 834–844. http://dx.doi.org/10.1016/j.mri.2009.01.005.

Özarslan, E., Koay, C.G., Shepherd, T.M., Basser, P.J., 2009b. Intracellular volume revealed by diffusion-weighted MRI. Magn. Reson. Mater. Phy. 22 (Suppl. 1), 37.

Özarslan, E., Koay, C.G., Shepherd, T.M., Blackband, S.J., Basser, P.J., 2009c. Simple harmonic oscillator based reconstruction and estimation for three-dimensional q-space MRI. Proc Intl Soc Mag Reson Med, vol. 17, p. 1396.

Özarslan, E., Shemesh, N., Koay, C.G., Cohen, Y., Basser, P.J., 2011. Nuclear magnetic resonance characterization of general compartment size distributions. New J. Phys. 13, 15010. http://dx.doi.org/10.1088/1367-2630/13/1/015010.

Özarslan, E., Shepherd, T.M., Koay, C.G., Blackband, S.J., Basser, P.J., 2012. Temporal scaling characteristics of diffusion as a new MRI contrast: findings in rat hippocampus. Neuroimage 60 (2), 1380–1393. http://dx.doi.org/10.1016/j.neuroimage.2012.01.105.

Özarslan, E., Koay, C.G., Basser, P.J., 2013. Simple harmonic oscillator based reconstruction and estimation for one-dimensional *q*-space magnetic resonance (1D-SHORE). In: Andrews, T.D., Balan, R., Benedetto, J.J., Czaja, W., Okoudjou, K.A. (Eds.), Excursions in Harmonic Analysis: The February Fourier Talks at the Norbert Wiener Center. Applied and Numerical Harmonic Analysis, vol. 2. Springer Science+Business Media, New York, pp. 373–400.

Ozcan, A., 2010. A new model for diffusion weighted MRI: complete Fourier direct MRI. Conf. Proc. IEEE Eng. Med. Biol. Soc. 2710–2713. http://dx.doi.org/10.1109/IEMBS.2010.5626530.

Pajevic, S., Pierpaoli, C., 1999. Color schemes to represent the orientation of anisotropic tissues from diffusion tensor data: application to white matter fiber tract mapping in the human brain. Magn. Reson. Med. 42 (3), 526–540.

Palazzi, X., Bordier, N., 2008. The Marmoset Brain in Stereotaxic Coordinates. Springer Science+Business Media, New York, NY.

Paulsen, J.L., Cho, H., Cho, G., Song, Y.-Q., 2011. Acceleration of multi-dimensional propagator measurements with compressed sensing. J. Magn. Reson. 213 (1), 166–170. http://dx.doi.org/10.1016/j.jmr.2011.08.025.

Pawula, R.F., 1987. Approximating distributions from moments. Phys. Rev. A 36, 4996–5007.

Pierpaoli, C., Basser, P.J., 1996. Toward a quantitative assessment of diffusion anisotropy. Magn. Reson. Med. 36 (6), 893–906.

Pluhar, Z., Tolar, J., 1961. Transformation matrix for the isotropic harmonic oscillator eigenvectors in $\{n_1n_2n_3\}$ and $\{nlm\}$ representations. Czech. J. Phys. B 14, 287–293.

Rathi, Y., Michailovich, O., Setsompop, K., Bouix, S., Shenton, M.E., Westin, C.-F., 2011. Sparse multi-shell diffusion imaging. Lect. Notes Comput. Sci 14 (II), 58–65.

Schwartz, S.C., 1967. Estimation of probability density by an orthogonal series. Ann. Math. Stat. 38, 1261–1265.

Shepherd, T.M., Özarslan, E., King, M.A., Mareci, T.H., Blackband, S.J., 2006. Structural insights from high-resolution diffusion tensor imaging and tractography of the isolated rat hippocampus. Neuroimage 32 (4), 1499–1509. http://dx.doi.org/10.1016/j.neuroimage.2006.04.210.

Stejskal, E.O., 1965. Use of spin echoes in a pulsed magnetic-field gradient to study anisotropic, restricted diffusion and flow. J. Chem. Phys. 43 (10), 3597–3603.

Stejskal, E.O., Tanner, J.E., 1965. Spin diffusion measurements: spin echoes in the presence of a time-dependent field gradient. J. Chem. Phys. 42 (1), 288–292.

Tournier, J.D., Calamante, F., Gadian, D.G., Connelly, A., 2004. Direct estimation of the fiber orientation density function from diffusion-weighted MRI data using spherical deconvolution. Neuroimage 23, 1176–1185.

Tuch, D.S., 2004. Q-ball imaging. Magn. Reson. Med. 52, 1358–1372.

Walter, G.G., 1977. Properties of Hermite series estimation of probability density. Ann. Stat. 5, 1258–1264.

Wedeen, V.J., Hagmann, P., Tseng, W.-Y.I., Reese, T.G., Weisskoff, R.M., 2005. Mapping complex tissue architecture with diffusion spectrum magnetic resonance imaging. Magn. Reson. Med. 54 (6), 1377–1386. http://dx.doi.org/10.1002/mrm.20642.

Wu, Y.-C., Alexander, A.L., 2007. Hybrid diffusion imaging. Neuroimage 36 (3), 617–629. http://dx.doi.org/10.1016/j.neuroimage.2007.02.050.

Ye, W., Portnoy, S., Entezari, A., Blackband, S.J., Vemuri, B.C., 2012. An efficient interlaced multi-shell sampling scheme for reconstruction of diffusion propagators. IEEE Trans. Med. Imaging 31 (5), 1043–1050. http://dx.doi.org/10.1109/TMI.2012.2184551.

Yeh, F.-C., Wedeen, V.J., Tseng, W.-Y.I., 2011. Estimation of fiber orientation and spin density distribution by diffusion deconvolution. Neuroimage 55 (3), 1054–1062.